Monthly Notices
of the
ROYAL ASTRONOMICAL SOCIETY

MNRAS **489,** 2330–2354 (2019) doi:10.1093/mnras/stz806

S-band Polarization All-Sky Survey (S-PASS): survey description and maps

E. Carretti [1,2,3★] M. Haverkorn,[4] L. Staveley-Smith [5] G. Bernardi,[1,6,7] B. M. Gaensler [8] M. J. Kesteven,[3] S. Poppi,[2] S. Brown,[9] R. M. Crocker [10] C. Purcell,[11,12] D. H. F. M. Schnitzler[13] and X. Sun[14]

[1]*INAF Istituto di Radioastronomia, Via Gobetti 101, 40129 Bologna, Italy*
[2]*INAF Osservatorio Astronomico di Cagliari, Via della Scienza 5, 09047 Selargius (CA), Italy*
[3]*CSIRO Astronomy and Space Science, PO Box 76, Epping, NSW 1710, Australia*
[4]*Department of Astrophysics/IMAPP, Radboud University Nijmegen, PO Box 9010, 6500 GL Nijmegen, the Netherlands*
[5]*International Centre for Radio Astronomy Research, University of Western Australia, Crawley, WA 6009, Australia*
[6]*SKA SA, 3rd Floor, The Park, Park Road, Pinelands 7405, South Africa*
[7]*Department of Physics and Electronics, Rhodes University, PO Box 94, Grahamstown 6140, South Africa*
[8]*Dunlap Institute for Astronomy and Astrophysics, University of Toronto, 50 George St, Toronto, ON M5S 3H4, Canada*
[9]*Department of Physics & Astronomy, The University of Iowa, Iowa City, Iowa 52245, USA*
[10]*Research School of Astronomy and Astrophysics, Australian National University, Canberra, Australia*
[11]*Research Centre for Astronomy, Astrophysics, and Astrophotonics, Macquarie University, NSW 2109, Australia*
[12]*Sydney Institute for Astronomy, School of Physics, The University of Sydney, NSW 2006, Australia*
[13]*Bendenweg 51, 53121 Bonn, Germany*
[14]*Department of Astronomy, Yunnan University, and Key Laboratory of Astroparticle Physics of Yunnan Province, Kunming 650091, China*

Accepted 2019 March 14. Received 2019 March 15; in original form 2018 October 2

ABSTRACT

We present the S-Band Polarization All Sky Survey (S-PASS), a survey of polarized radio emission over the southern sky at Dec. $<-1^\circ$ taken with the Parkes radio telescope at 2.3 GHz. The main aim was to observe at a frequency high enough to avoid strong depolarization at intermediate Galactic latitudes (still present at 1.4 GHz) to study Galactic magnetism, but low enough to retain ample signal-to-noise ratio (S/N) at high latitudes for extragalactic and cosmological science. We developed a new scanning strategy based on long azimuth scans and a corresponding map-making procedure to make recovery of the overall mean signal of Stokes *Q* and *U* possible, a long-standing problem with polarization observations. We describe the scanning strategy, map-making procedure and validation tests. The overall mean signal is recovered with a precision better than 0.5 per cent. The maps have a mean sensitivity of 0.81 mK on beam-size scales and show clear polarized signals, typically to within a few degrees of the Galactic plane, with ample S/N everywhere (the typical signal in low-emission regions is 13 mK and 98.6 per cent of pixels have S/N > 3). The largest depolarization areas are in the inner Galaxy, associated with the Sagittarius Arm. We have also computed a rotation measure map combining S-PASS with archival data from the *Wilkinson Microwave Anisotropy Probe* (*WMAP*) and *Planck* experiments. A Stokes *I* map has been generated, with sensitivity limited to the confusion level of 9 mK.

Key words: magnetic fields – polarization – radiation mechanisms: non-thermal – methods: observational – Galaxy: structure – diffuse radiation.

1 INTRODUCTION

All-sky radio polarization surveys are extremely important for a number of scientific aims, ranging from the Galactic interstellar medium (ISM) to cosmology. Radio polarization observations allow the study of the magnetic fields of both the emitting source – either compact or extended – and the foreground medium. Ultrarelativistic electrons accelerated by magnetic fields emit synchrotron emission. The emission is intrinsically highly polarized (some 70 per cent), with polarization angle oriented by 90° compared with the magnetic field orientation on the plane of the sky. The polarization fraction

★ E-mail: carretti@ira.inaf.it

Table 1. Main characteristics and parameters of S-PASS.

Effective central frequency[1]	2303 MHz
Useful bandwidth[2]	168 MHz
Frequency ranges	2176–2216 MHz
	2272–2400 MHz
FWHM	8.9 arcmin
Flux density to brightness temperature gain	1.19 Jy K^{-1}
Channel bandwidth	0.5 MHz
Binned sub-band bandwidth	8 MHz
Sky coverage	Dec. $<-1^{\circ}$
Pixel size	3.4 arcmin
Sky projection	HEALPIX
Total observing time	1820 h
Mean Q, U beam-size pixel rms sensitivity	0.815 mK
Stokes I confusion limit	9 mK
Flux density calibration accuracy	5%
Instrumental polarization	$< 0.05\%$
Mean source position rms error	33 arcsec
Map systematic pointing error	5.6 arcsec

[1] Mean frequency of used frequency channels. [2] After RFI channel flagging.

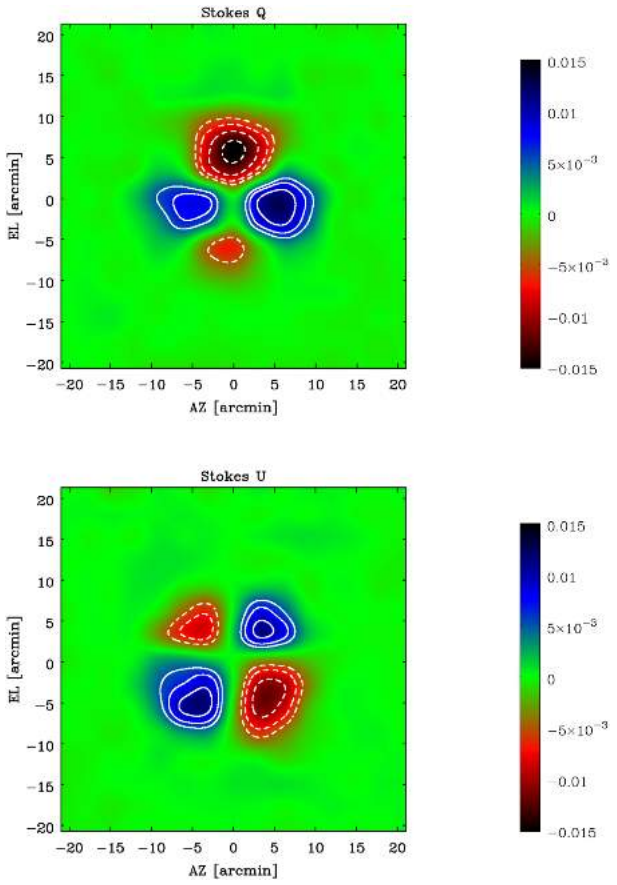

Figure 1. Instrumental polarization beam pattern for Stokes Q (top) and U (bottom) measured using the unpolarized source PKS B1934−638. Unit is fractional polarization. Contour lines are for positive (solid) and negative (dashed) values, starting from ±0.5 per cent and scaling with a $\sqrt{2}$ factor.

and its variation with frequency provide key information about a magnetized medium. Net polarization requires the field to be ordered to some degree; in a fully turbulent medium, the field is completely tangled and the resulting emission unpolarized. A magnetic field with a projected direction on the plane of the sky

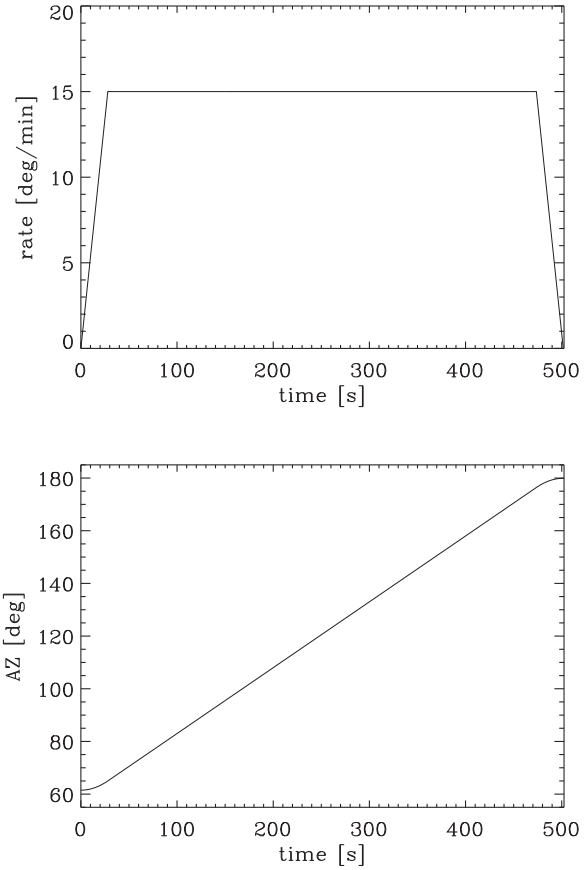

Figure 2. Scan rate (top) and azimuth behaviour (bottom) versus time for a forward eastward scan. The phase at cruise speed of $15^{\circ}\,\mathrm{min}^{-1}$ is preceded and followed by a 28-s ramp-up and down at constant acceleration.

that varies along the line of sight can also depolarize the emission. This is a purely geometrical effect, independent of the observing frequency.

The polarization fraction indicates the relative strength of isotropic turbulent and ordered components, while its behaviour with frequency provides information about the conditions of the source medium and its magnetic field (e.g. Farnes, Gaensler & Carretti 2014; Lamee et al. 2016).

Faraday rotation (FR) rotates the observed polarization angle ϕ in proportion to wavelength squared, λ^2, as the polarized emission passes through a magnetoionic medium consisting of free electrons immersed in a magnetic field:

$$\phi = \phi_0 + \mathrm{RM}\,\lambda^2\,, \tag{1}$$

where ϕ_0 is the radiation intrinsic polarization angle (in the case of no FR or $\lambda = 0$) and RM measures the field component parallel to the line of sight $B_{\shortparallel}$ weighted by the free electron density n_{e}:

$$\mathrm{RM}\,[\mathrm{rad\,m^{-2}}] = 821 \int_{\mathrm{source}}^{\mathrm{observer}} n_{\mathrm{e}}\,[\mathrm{cm^{-3}}]\; B_{\shortparallel}\,[\mu\mathrm{G}]\,\mathrm{d}l\,[\mathrm{kpc}]\,. \tag{2}$$

From these relations, FR can be used to infer information about the magnetic field. In particular, the observed rotation of the polarization angle with frequency, a fit to multifrequency observations or the application of the RM-synthesis algorithm (Brentjens & de Bruyn 2005) will give an estimate of the RM, which, in turn, gives information on the magnetic field along the line of sight. FR can also have a destructive effect. If the polarization angle variation

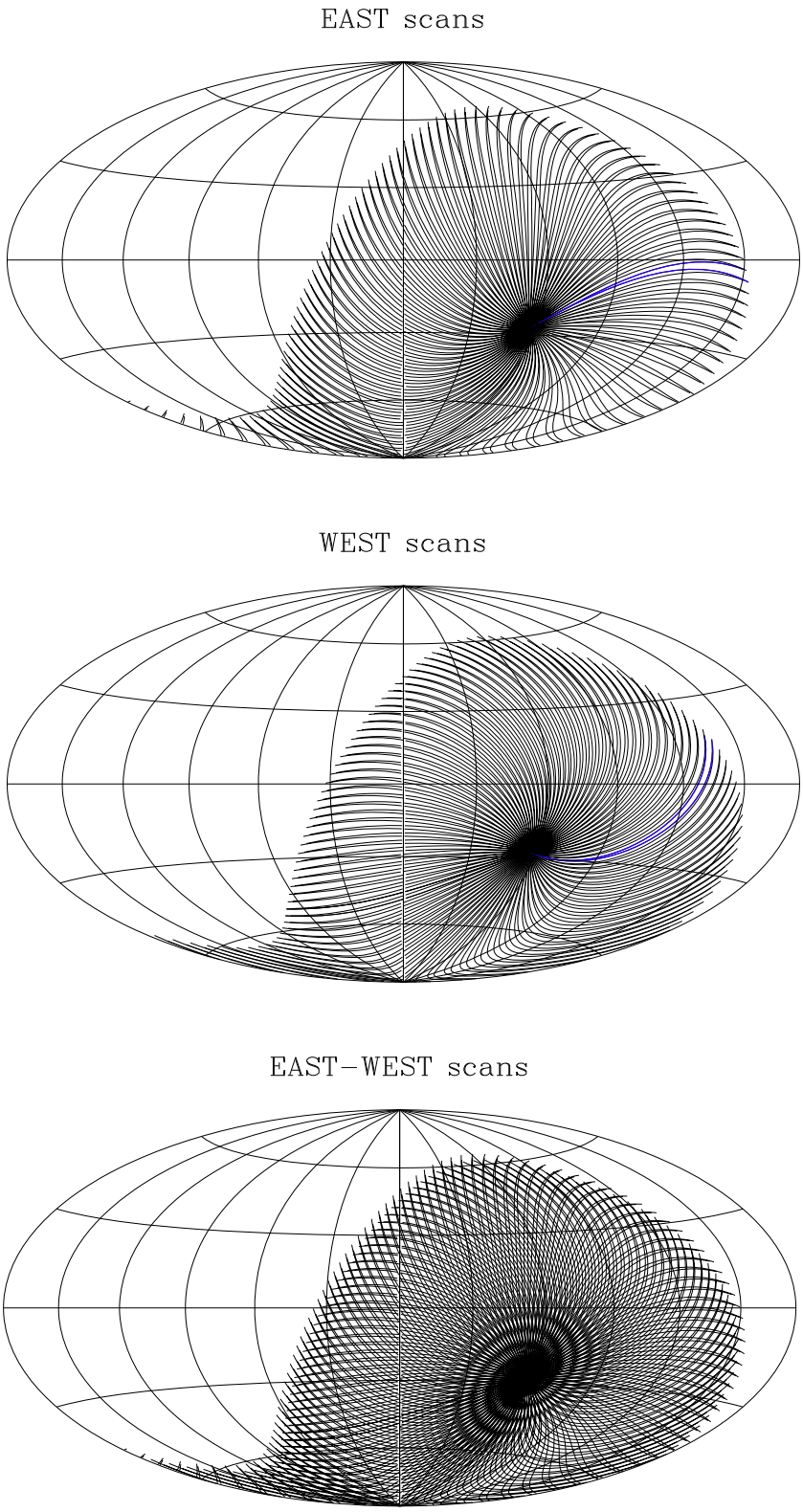

Figure 3. *Top:* full sequence of east scans as taken with an uninterrupted observation of 24 h sidereal time. Positions are shown in Galactic coordinates in Aitoff projection with longitude 0 at the centre, north up and west to the right. Note that the loop is closed, so, were the observation to continue for another 24 h, the entire sequence would repeat exactly. A single back-and-forth scan pair is highlighted in blue. *Middle:* as for the top panel, except for west scans. *Bottom:* the two full sequences of east and west scans are plotted together to show how they cross each other.

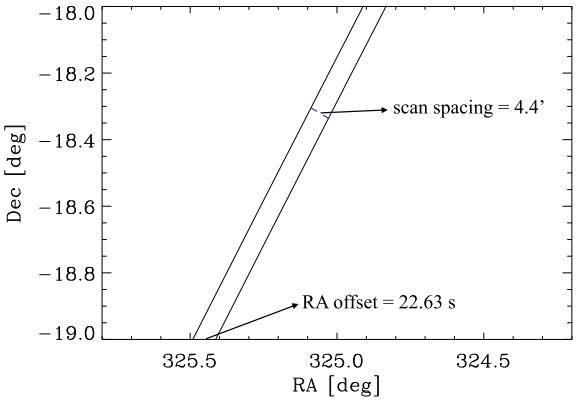

Figure 4. Portion of two east scans of two different zigzag sequences spaced by just one RA/LST offset unit $d_{\mathrm{RA_{east}}} = 21.63$ s, realizing a spacing of 4.38 arcmin at the declination where the spacing is largest (Dec. $\sim -18.4^\circ$).

within the frequency channel, the telescope beam or the emitting region is too large, FR causes signal cancellation (depolarization, e.g. see Burn 1966).

The optimal observing frequency depends on the region, its complexity and the amount of RM involved. Low-frequency observations are more sensitive to RM, but are more prone to depolarization. High frequencies are less affected by depolarization and therefore reveal much more polarized emission, even close to the Galactic plane, where emission is complex. They also return angles closer to the intrinsic polarization angle, and therefore inform us more directly of the orientation of the magnetic field on the plane of the sky. Ideally, observations over a broad frequency range are required.

For nearly three decades from the mid-1970s, the only available polarization surveys were the collection by Brouw & Spoelstra (1976), covering five frequencies from 408–1411 MHz, but sparsely and irregularly sampled and with coarse resolution (a few degrees). In the mid 2000s, the first all-sky survey at 1.4 GHz by the Dominion Radio Astronomical Observatory (DRAO) and Villa Elisa telescopes with 36-arcmin resolution appeared (Wolleben et al. 2006; Testori, Reich & Reich 2008), followed at 23 GHz by the *Wilkinson Microwave Anisotropy Probe* (*WMAP*) with $\sim 1^\circ$ resolution (Page et al. 2007; Bennett et al. 2013). Together, these provided the astronomy community with its first comprehensive view of the polarized sky. However, that view was incomplete. Depolarization is significant at low frequency. Maps made by Carretti et al. (2005) from Brouw & Spoelstra (1976) data show that at 408 MHz most of the sky is depolarized, with the exception of the Galactic polar caps. With increasing frequency, the depolarization starts to disappear and signal appears at progressively lower latitudes. The 1.4-GHz maps of Wolleben et al. (2006) and Testori et al. (2008) show that polarized emission is still totally depolarized at $|b| < 30^\circ$ and with Faraday modulation visible up to $|b| = 50^\circ$ (Carretti et al. 2010), with the exception of the Fan region in the outer Galaxy at longitude $l \sim 135^\circ$, where the disc RM is close to zero and Faraday effects are smaller. At the other end of the radio spectrum, *WMAP* high-frequency polarization observations resulted in the first all-sky image without FR. However, the *WMAP* image suffered from poor signal-to-noise ratio (S/N), especially in the halo at mid and high latitudes, and is insufficient for conducting high-precision studies of cosmic magnetism and polarized cosmic microwave background (CMB) foregrounds. Moreover, this image showed that a finer resolution was required to help beat depolarization in high RM

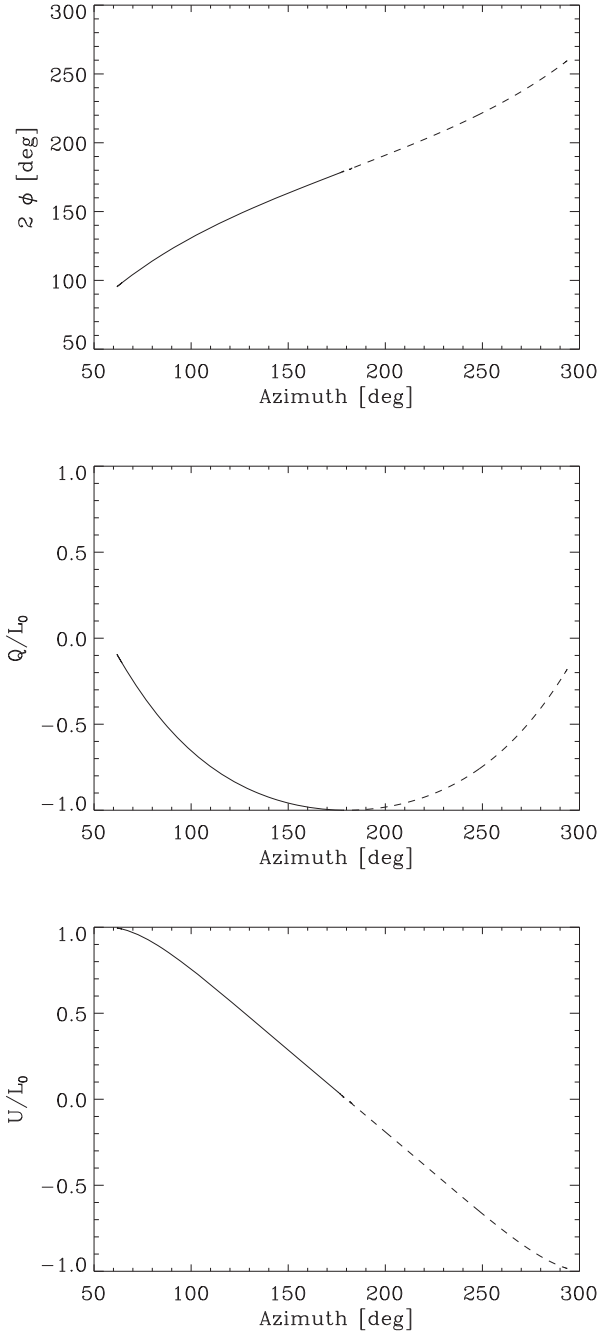

Figure 5. *Top*: range covered in the east (solid) and west (dashed) scans of S-PASS of 2 × the parallactic angle (2ϕ), which is the angle the two Stokes parameters Q and U are modulated with. *Middle*: example of Stokes Q behaviour along east (solid) and west scans (dashed) modulated by the variation of ϕ of the top panel. Stokes Q is normalized to the polarized emission amplitude L_0. The case of emission polarization angle $\theta_0 = 0^\circ$ is shown. *Bottom*: as for middle, panel except for Stokes U.

regions and to reveal full details of the Galactic ISM and Galactic objects.

This article presents the S-band Polarization All Sky Survey (S-PASS), a survey of the radio polarized emission at 2.3 GHz in the southern sky at Dec $< -1^\circ$ conducted with the Parkes radio telescope at an angular resolution of 8.9 arcmin. The frequency is a compromise: higher than 1.4 GHz allows us to beat FR in

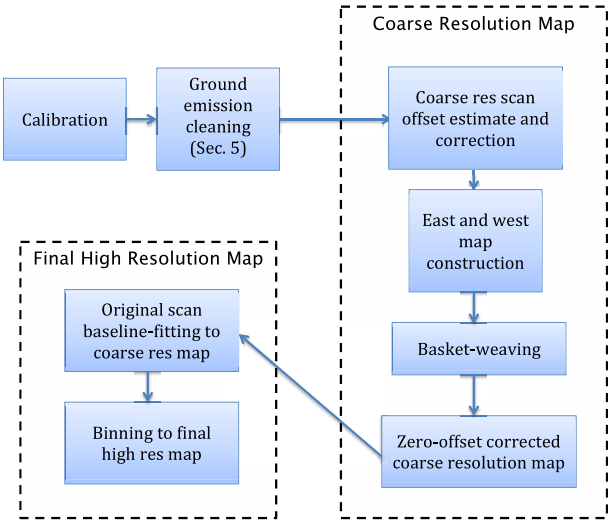

Figure 6. Block diagram of the map-making procedure.

the Galactic disc and to reveal Galactic emission and structure in the disc and at the disc–halo transition. However, the frequency is still low enough to retain ample S/N in low-emission areas at high Galactic latitude, which is required for high-precision magnetism studies in the Galactic halo and for CMB foreground analysis. The angular resolution of S-PASS is four times better than the DRAO and Villa Elisa maps (and six times than *WMAP*'s), delivering a much more detailed view of the sky. Although S-PASS is designed and optimized for polarization measurements, we have also taken total intensity data and produced a Stokes *I* sky map.

The science that can be addressed given the S-PASS characteristics is very diverse. Applications include the following.

(i) Galactic magnetism, which can be studied through polarization angles and RMs. In particular, large-scale Galactic magnetic field models can be optimized by fitting to these data (e.g. Sun et al. 2008; Jansson & Farrar 2012).

(ii) Study of polarized emission from the Galactic disc within $|b| < 30^\circ$, which can reveal structures in the disc and at the disc–halo transition, otherwise hidden by depolarization at lower frequencies. Structures such as loops and lobes have much more contrast in polarization than in total intensity, making them easier to identify and analyse (e.g. see Vidal et al. 2015; Carretti et al. 2013a). S-PASS reveals polarized emission down to a few degrees from the Galactic plane, even uncovering new structures in the inner Galaxy (Carretti et al. 2013a; Thomson et al. 2018).

(iii) ISM turbulence, which can be identified and studied with the polarization-gradient technique (Gaensler et al. 2011). This has previously been applied to limited areas (e.g. Gaensler et al. 2011; Herron et al. 2017), but the area, sensitivity and resolution of S-PASS render it possible to construct an image of turbulence throughout the Milky Way (Iacobelli et al. 2014; Robitaille et al. 2017).

(iv) The search for the B-mode of CMB polarization is one of the most important topics in astrophysics today. Detection of this signal would constitute discovery of the primeval cosmological gravitational-wave background emitted at the time of inflation and would discriminate between the plethora of proposed inflation models. B-mode CMB polarization detection is hampered by Galactic foregrounds, of which synchrotron is one of the most important and is stronger than the cosmological signal (e.g. Carretti et al. 2010; Krachmalnicoff et al. 2016). The high S/N, low FR and high resolution of S-PASS are ideal to characterize this foreground precisely, estimate its impact on CMB experiments and allow for the optimization of CMB observing strategies. Moreover, in combination with data at other frequencies (e.g. C-Band All Sky Survey (C-BASS) (Jones et al. 2018) and Q-U-I JOint TEnerife (QUIJOTE) (Poidevin et al. 2018)), S-PASS data allow for the construction of precise templates with which to reduce pollution by the Galactic foreground significantly and thereby open up the possibility of detection of the gravitational-wave background, even for pessimistic models.

(v) The S-PASS angular resolution has made it possible to produce a catalogue of a few thousand polarized, compact sources (Schnitzeler et al. 2019). The analysis of catalogues with hundreds of sources shows weak evidence for the evolution of magnetism for extragalactic radio sources (e.g. Farnes et al. 2014; Lamee et al. 2016). With an order of magnitude more sources, unambiguous detection is possible.

(vi) The radio-emitting intracluster medium (ICM) in galaxy clusters, including radio haloes and relics, is usually observed with compact interferometers with good sensitivity to extended emission and sufficient resolution to discriminate between this emission and the blending of compact sources. However, the ICM of nearby clusters can stretch over angular scales that interferometers miss or at which they have poor sensitivity. The risk, therefore, is underestimating such structures (because a significant part of their extended flux is missed), which, in turn, leads to incorrect inference of the total energetics and the consequent physical misinterpretation of cluster phenomena. Single-dish telescopes have an unparalleled sensitivity to extended emission, retaining information on all angular scales. As previously shown (Brown & Rudnick 2011; Loi et al. 2017; Vacca et al. 2018), observations with large, single-dish telescopes of a size that matches the minimum interferometer baseline are thus essential to obtain a full picture of large structures. S-PASS is in an excellent position to contribute to this effort with its high sensitivity and resolution (Carretti et al. 2013b).

(vii) In addition to ICM diffuse emission, searches are underway for synchrotron emission from the Cosmic Web. This would probe the flow of gas into filaments and from filaments to clusters, which are the nodes of the Cosmic Web. Moreover, some 50 per cent of all cosmic baryons are expected to be in filaments (Nicastro et al. 2018) and synchrotron emission detection is essential to test the current scenario of structure formation. Single-dish telescopes with large dishes are ideal for such a search, thanks to their sensitivity to extended emission and resolution. The transverse size of the filaments of the local Cosmic Web is some 10 arcmin. S-PASS, with its beam of 8.9 arcmin, is perfectly suited for finding these. Upper limits have been found so far with correlation techniques between radio emission and cosmic web tracers (e.g. Brown et al. 2017; Vernstrom et al. 2017) and a possible detection of diffuse synchrotron emission from a filament has recently been reported using the 64-m Sardinia Radio Telescope in combination with interferometric data to subtract blended compact sources (Vacca et al. 2018).

S-PASS is part of a 'Golden Age' of single-dish polarization surveys. The radio polarization community is making a significant effort to map the sky over a broad frequency range and fill the gaps in all-sky, diffuse polarized emission information. The Global MagnetoIonic Medium Survey (GMIMS) aims at mapping the entire sky from 300–1800 MHz with high frequency resolution (Wolleben et al. 2009). Observations have been completed for the

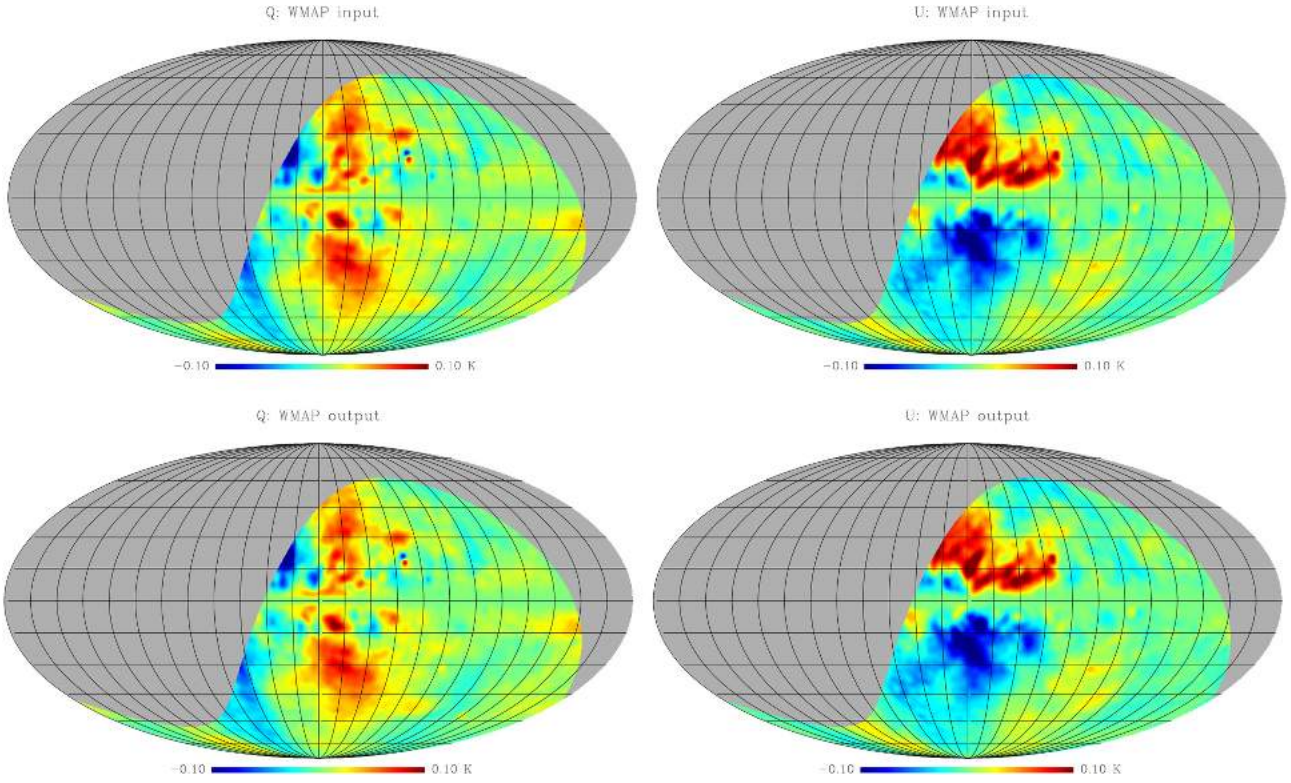

Figure 7. *Top*: Stokes Q (left) and U map (right) used as input maps for the simulation to test the capability of the map-making procedure to recover the real sky. The images are in Galactic coordinates centred on the Galactic Centre, with gridlines spaced by 15°. Note that the IAU convention of polarization angles is used here and the Stokes U map shown here has the sign changed compared with the original *WMAP* data set. *Bottom*: as for the top panels, but for the output maps resulting from the map-making procedure applied to the simulated observations extracted from the input maps.

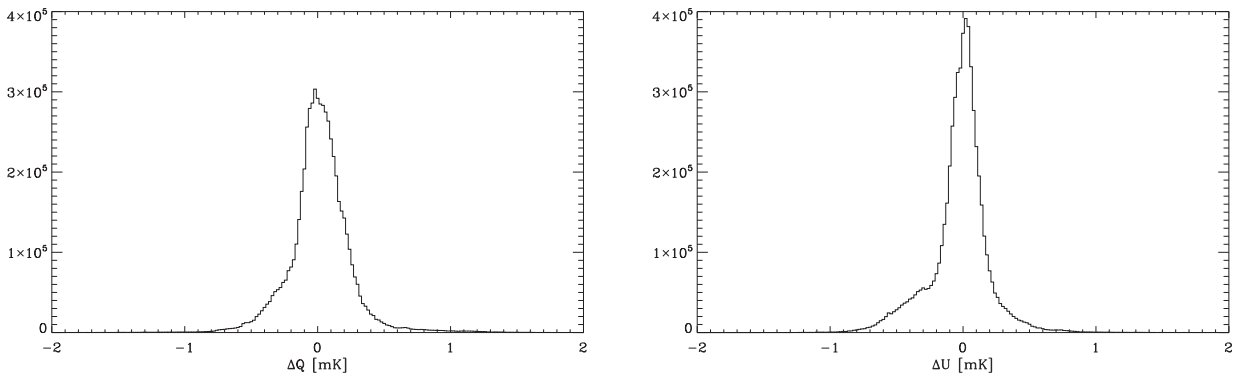

Figure 8. Distribution of the difference between input and reconstructed maps in the case with no instrumental noise, from which one may estimate the scale of errors arising solely from the map-making procedure: Stokes Q (left) and U (right).

GMIMS North High-Band survey, covering 1300–1800 MHz with the 26-m DRAO telescope (Wolleben et al. 2010), and the GMIMS South Low-Band survey, covering 300–900 MHz (Wolleben et al. 2019), and GMIMS South High-Band survey, covering 1300–1800 MHz (also known as Southern Twenty-centimeter All-sky Polarization Survey (STAPS): Haverkorn 2015), both with the Parkes radio telescope and using the same observing strategy developed by S-PASS. GMIMS and S-PASS complement each other: GMIMS is more focused on high RM sensitivity and the realization of Faraday tomography, while S-PASS is more focused on reducing depolarization and Faraday effects. C-BASS (Jones et al. 2018) is an all-sky survey at 5 GHz, thus with a higher frequency than S-PASS, but with lower S/N and coarser resolution. QUIJOTE (Poidevin et al. 2018) aims at observing the northern sky at 10–20 GHz with resolution similar to C-BASS. The future combination of S-PASS, C-BASS and QUIJOTE data holds out the promise of a high-accuracy synchrotron emission map for high-precision CMB foreground cleaning. Finally, *Planck* has delivered a polarization map at 30 GHz with S/N similar to *WMAP*, but finer angular resolution (Planck Collaboration 2018).

This article presents the S-PASS survey, its major features, observations, map-making algorithm and validation tests, residual contamination and maps. The scientific utilization of the data

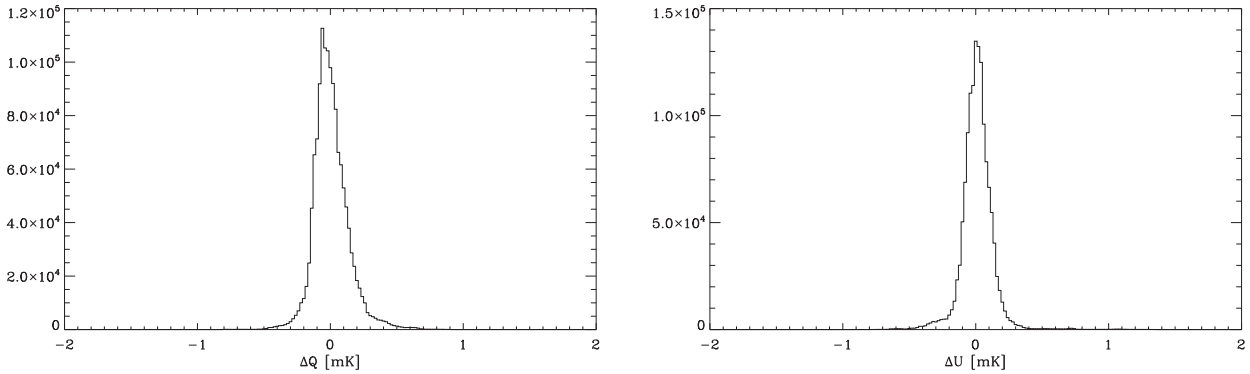

Figure 9. As for Fig. 8, except only for areas with polarized emission $L < 10$ mK. This restriction allows for a more accurate estimate of the performance of the map-making procedure in low-emission regions.

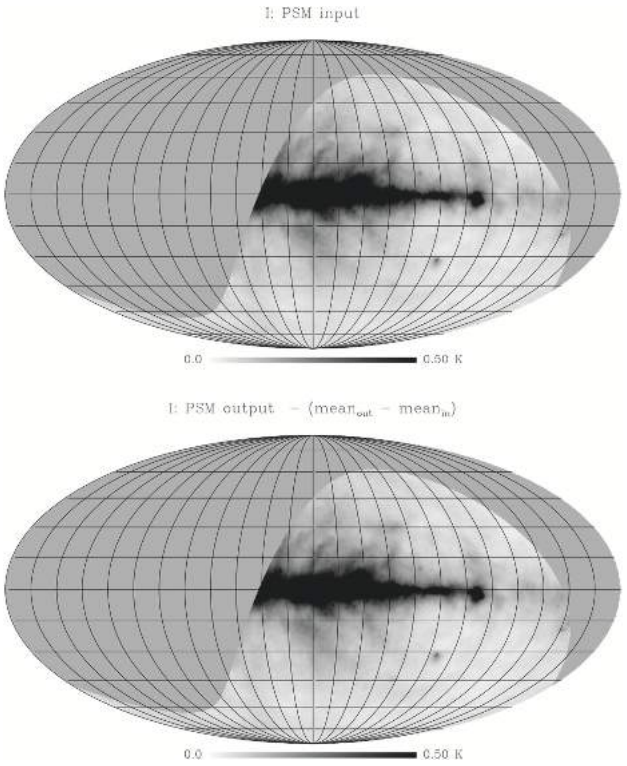

Figure 10. *Top*: Stokes *I* input map used in the simulation to test the map-making procedure. The images are in Galactic coordinates centred on the Galactic Centre, grid lines are spaced by 15°. *Bottom*: as for the top panel, but for an output map that is the result of the map-making procedure applied to the simulated observations extracted from the input map. The mean value of the input map is lost, so the map shown here is offset by the same amount to show better how other features were recovered.

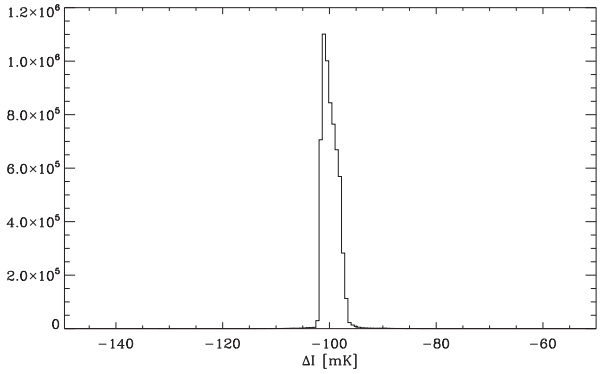

Figure 11. Distribution of the difference between Stokes *I* input and the reconstructed map in the no instrumental noise case. Note that there is an offset by about −100 mK, evidence of mean signal loss.

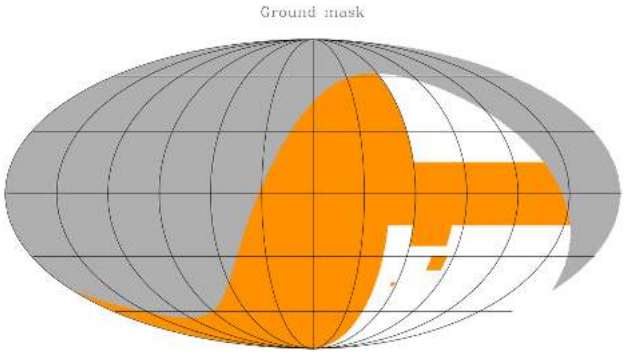

Figure 12. Area used to estimate the ground emission (white). The rest of the observed areas (orange in the online version) was masked out. The image is in Galactic coordinates centred on the Galactic Centre, grid lines are spaced by 30°.

is beyond the scope of this article and has been described in separate articles, published and in progress. In this article we describe and publicly release the data binned in one broad frequency band from all useful channels. A further article will describe the multifrequency data cube.

Throughout the article, we use the International Astronomical Union (IAU) convention for polarization angles (PA), as normally used in astrophysics: PA is 0° for vectors pointing north and increases eastward. Note that this differs from the convention used in some experiments, e.g. *WMAP* and *Planck*, where PA increases westward.

The article is organized as follows: Section 2 describes observations, calibration and the main data features, Section 3 covers the observing strategy and its design, Section 4 describes the map-making algorithm and its tests and Section 5 covers the ground-emission estimate and subtraction. In Section 6, we show the maps obtained from S-PASS data, together with an analysis of the signal distribution and main features. We also measure and display a RM map of the diffuse emission that combines S-PASS, *WMAP* and *Planck* data. Section 7 gives a summary of the scientific results obtained so far using S-PASS data and described in separate articles

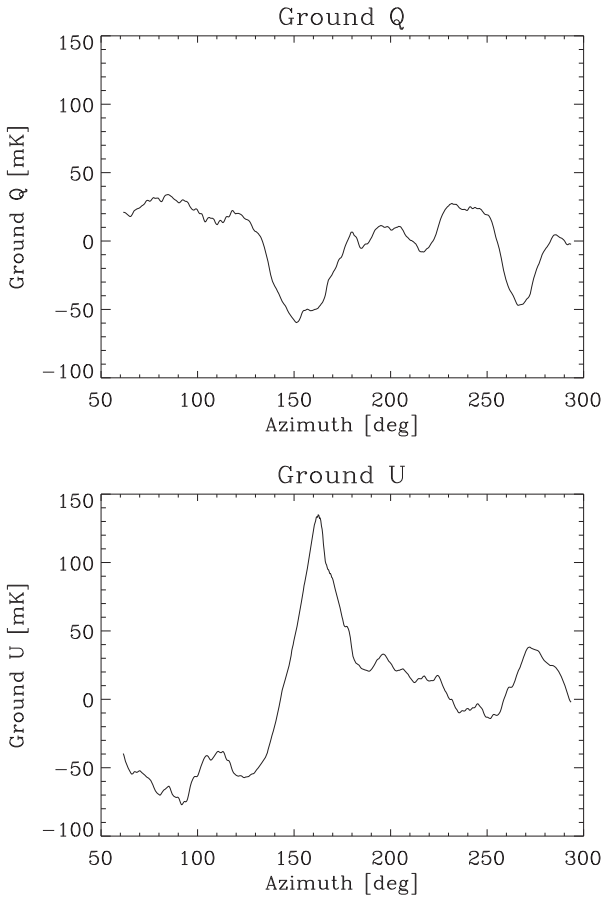

Figure 13. Ground emission profile for Stokes Q (top) and U (bottom) versus the azimuth range covered by the S-PASS scans.

and Section 8 lists the data set we will release, while Section 9 presents our summary and conclusions.

2 OBSERVATIONS AND CALIBRATIONS

Observations were conducted with the Parkes radio telescope, located in New South Wales, Australia. This is a primary focus, 64-m diameter telescope. Observations were carried out in eight sessions, either 17 or 18 nights each, from 2007 October–2009 July, spaced approximately three months apart (2007 October, 2008 January, 2008 April, 2008 July, 2008 October, 2009 January, 2009 April, 2009 July). Total observing time was approximately 1820 hours. The main observational parameters are reported in Table 1.

Observations were conducted at night, sunset-to-sunrise, to prevent solar contamination from side lobes, which are significant in polarization at this frequency when sensitivities of some 1 mJy beam^{-1} are desired (Carretti et al. 2005).

The bandpass was centred at a frequency of 2300 MHz, with 256-MHz nominal bandwidth. The bandpass filter limits the usable range to 2176–2400 MHz. The standard Parkes S-band receiver (*Galileo*) was used with a system temperature of $T_{\rm sys} \sim 20$ K. This is a circular polarization system delivering left-handed and right-handed circular polarization L and R, ideal for Stokes Q and U measurements with a single-dish telescope.

The feed is installed on-axis and illuminates the reflector with an edge taper of 19 dB. The beam has a full width at half-maximum

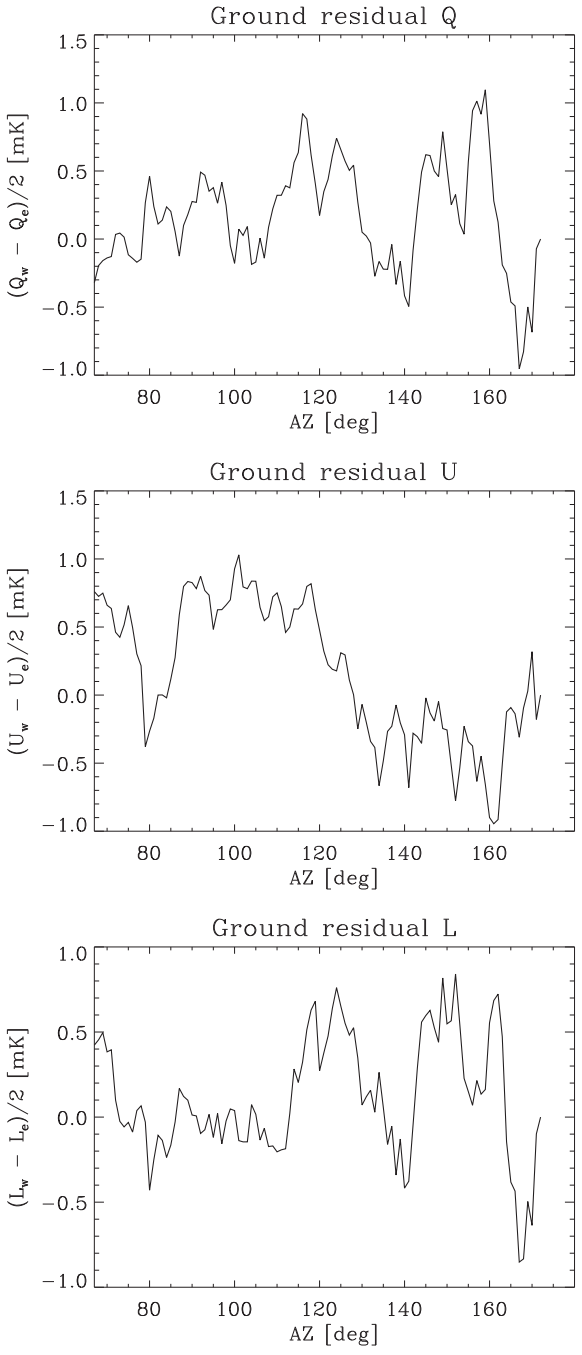

Figure 14. Ground-emission residual estimates after cleaning for Stokes Q (top), U (middle) and polarized intensity L (bottom). The quantity plotted is $(X_{\rm w}(360^\circ - {\rm AZ}) - X_{\rm e}({\rm AZ}))/2$, where $X = Q$, U and L, respectively – see equation (7). West scans at azimuth $(360 - {\rm AZ})$ see the same sky seen by east scans at azimuth, so the difference measures the residual contamination.

(FWHM) of 8.9 arcmin at 2.3 GHz and a first sidelobe at −31 dB, while the full-beam flux density to brightness temperature gain is $G = 1.19$ Jy K^{-1}.

The Digital Filter Bank Mark 3 (DFB3) backend was used, a digital spectropolarimeter recording the two autocorrelation products (RR^* and LL^*) and the complex cross-correlation product (RL^*) for full Stokes capability. A configuration with 256-

Table 2. Standard deviation (rms) of the estimated ground-emission residual of the polarized and total intensity emission shown in Figs 14 and 16 (Q, U, linear polarized intensity L and total intensity I).

	rms [mK]
Q	0.40
U	0.51
L	0.35
I	4.3

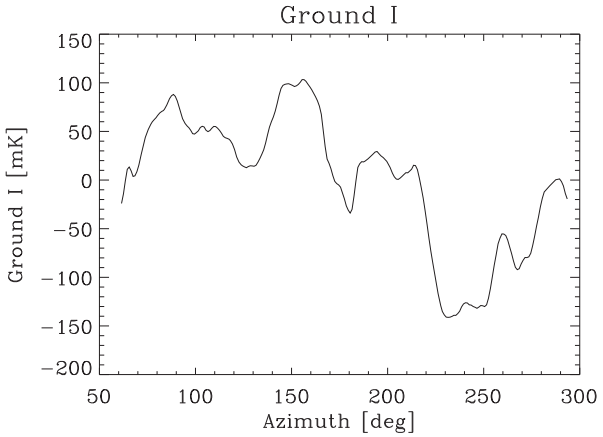

Figure 15. Ground-emission profile of Stokes I. Details are as for Fig. 13.

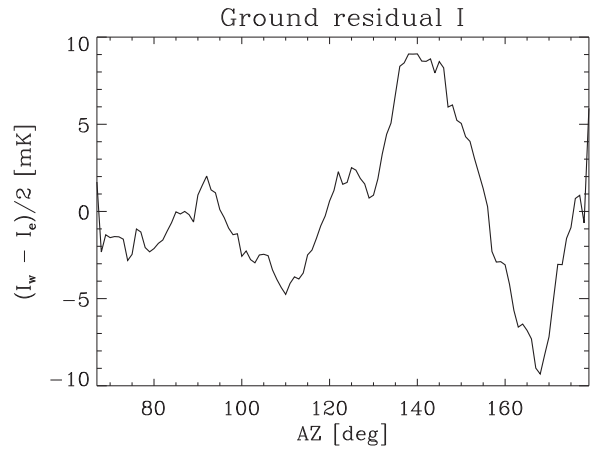

Figure 16. Ground-emission residual estimate after cleaning for Stokes I. Details are as for Fig. 14.

MHz bandwidth and 512 frequency channels, 0.5 MHz each, was used. The backend was based on 8-bit samplers for a large dynamic range. The channelization is based on a polyphase filter technique to ensure an impressive isolation between frequency channels (more than 60 dB between adjacent channels), giving negligible cross-contamination by in-band radio-frequency interference (RFI). This represents a leap in capability compared with the 13-dB isolation of the old generation of Fourier-based correlators.

Flux calibration was performed using PKS B1934−638. We assumed the flux density model of Reynolds (1994), which covers the range 0.4–9 GHz with an accuracy of 5 per cent (Bernardi et al. 2003). The source PKS B0407−658 was used as secondary calibrator. Flux calibration was performed for each frequency channel, effectively delivering a flat calibrated bandpass.

Data were binned in 8-MHz bins and, after RFI flagging, 21 bins were used, covering the ranges 2176–2216 and 2272–2400 MHz, for an effective central frequency of 2303 MHz and bandwidth of 168 MHz.

On-axis instrumental polarization calibration was performed using the flux calibrator PKS B1934−638[1] and Ori A (Gardner, Whiteoak & Morris 1975); these are assumed to be unpolarized down to 0.1 per cent. We measured a typical instrumental polarization of 1 per cent in each frequency channel, rising to 2 per cent at the two very ends of the band. Following this measurement, instrumental polarization was subtracted using the standard technique. Once calibrated and corrected, the residual instrumental polarization on individual frequency channels was within $<\sim$0.2 per cent, while, averaged over the entire 2176–2400 MHz band, it was better than 0.05 per cent. The fractional instrumental polarization is estimated as the measured Q and U response when observing the unpolarized calibrator divided by its Stokes I flux. Then, for each segment of data, that fraction of its Stokes I emission is subtracted from its measured Stokes Q and U.

The off-axis instrumental polarization pattern after on-axis calibration is reported in Fig. 1, measured using PKS B1934−638. The impact of this on scientific results is marginal: it does not affect polarization measurements of compact sources. For diffuse emission, the pattern of opposite-sign lobes leads to cancellation on scales larger than twice the beam size, with no significant residual effects (e.g. see Carretti et al. 2004; Murgia et al. 2016). We estimate residual instrumental polarization of 0.08 and 0.06 per cent for Stokes Q and U, respectively, when averaged over the instrumental polarization beam area, which represents the residual leakage of Stokes I into Q and U in the case of uniform emission on the beam scale. No deconvolution of the instrumental polarization beam was carried out for this data release.

Polarization angle calibration was performed using the sources PKS B0043–424 and 3C 138, assuming polarization angles of $PA_{0043} = 140^\circ$ and $PA_{3C138} = 169^\circ$, respectively (Broten, MacLeod & Vallee 1988; Perley & Buttler 2013). The calibration was performed on each frequency bin (8 MHz width) to make in-band depolarization negligible. We found that our data have a rotation of less than 3° over each 8-MHz bin before calibration, for a negligible depolarization smaller than 0.05 per cent. This reveals another obvious advantage of the modern spectropolarimetry: in-band phase equalization is no longer strongly required on the scale of the entire observing band – only on the scale of the individual frequency channel width. This relaxes the instrument design requirements significantly.

Pointing calibration was performed by the observatory staff at each session. Typical precision was better than 10 arcsec. Measured on the final data set, the position-error distribution of the compact sources identified in the maps has a mean and dispersion of 4.7 ± 24.7 arcsec in RA and 3.1 ± 22.4 arcsec in Dec. (Meyers et al. 2017). The dispersion (33 arcsec combined) is the mean root-mean-square (rms) position error of the individual sources, which

[1] http://www.narrabri.atnf.csiro.au/calibrators/calibrator_database_viewcal?source = 1934-638

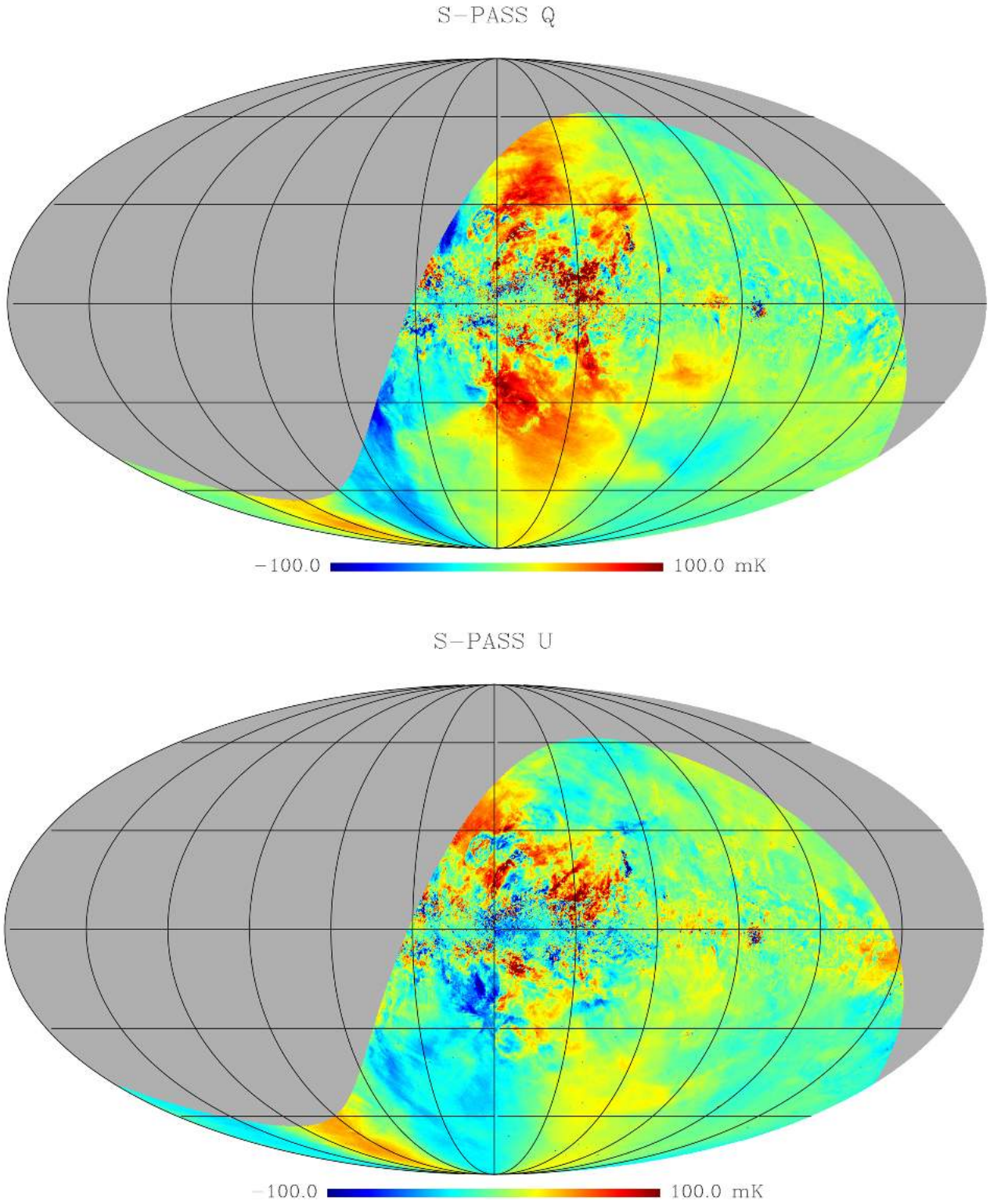

Figure 17. S-PASS maps of Stokes Q (top) and U (bottom). Maps are in Mollweide projection, Galactic coordinates, with the Galactic centre at the centre and longitude increasing leftward.

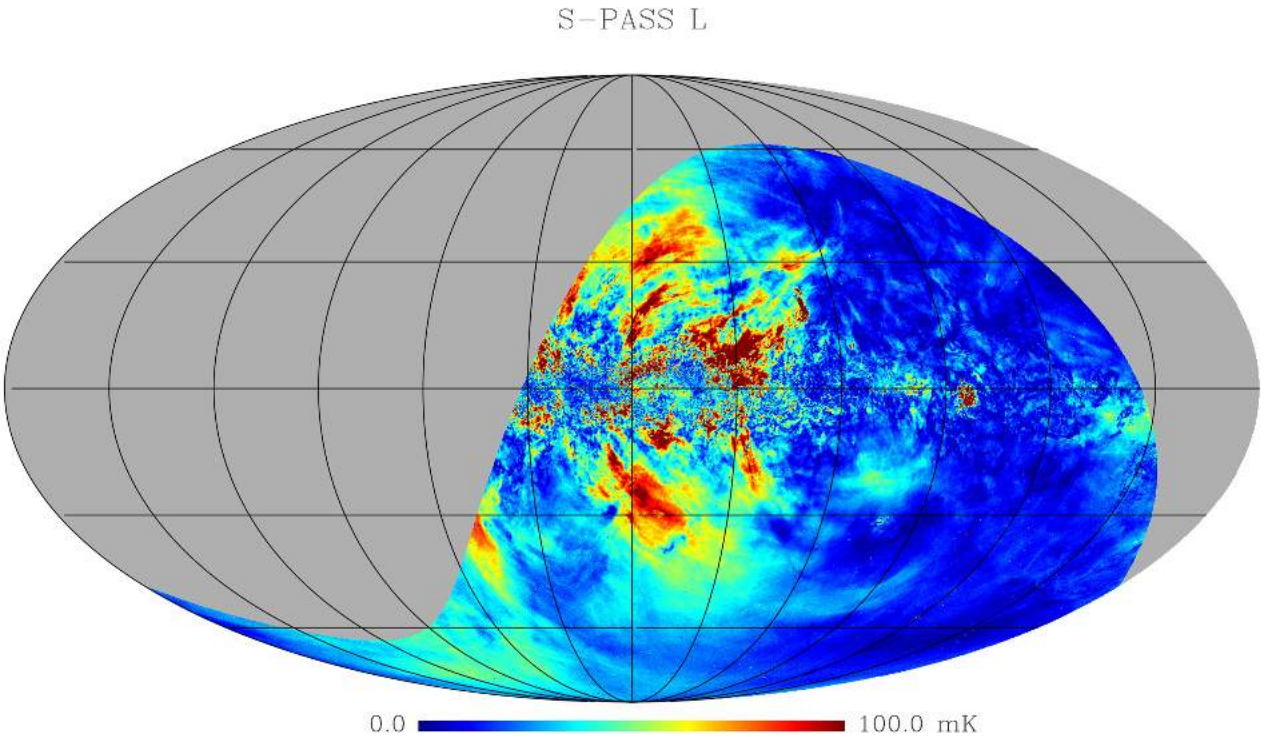

Figure 18. S-PASS map of linear polarized intensity *L*. The map is in Mollweide projection, Galactic coordinates, with the Galactic centre at the centre and longitude increasing leftward.

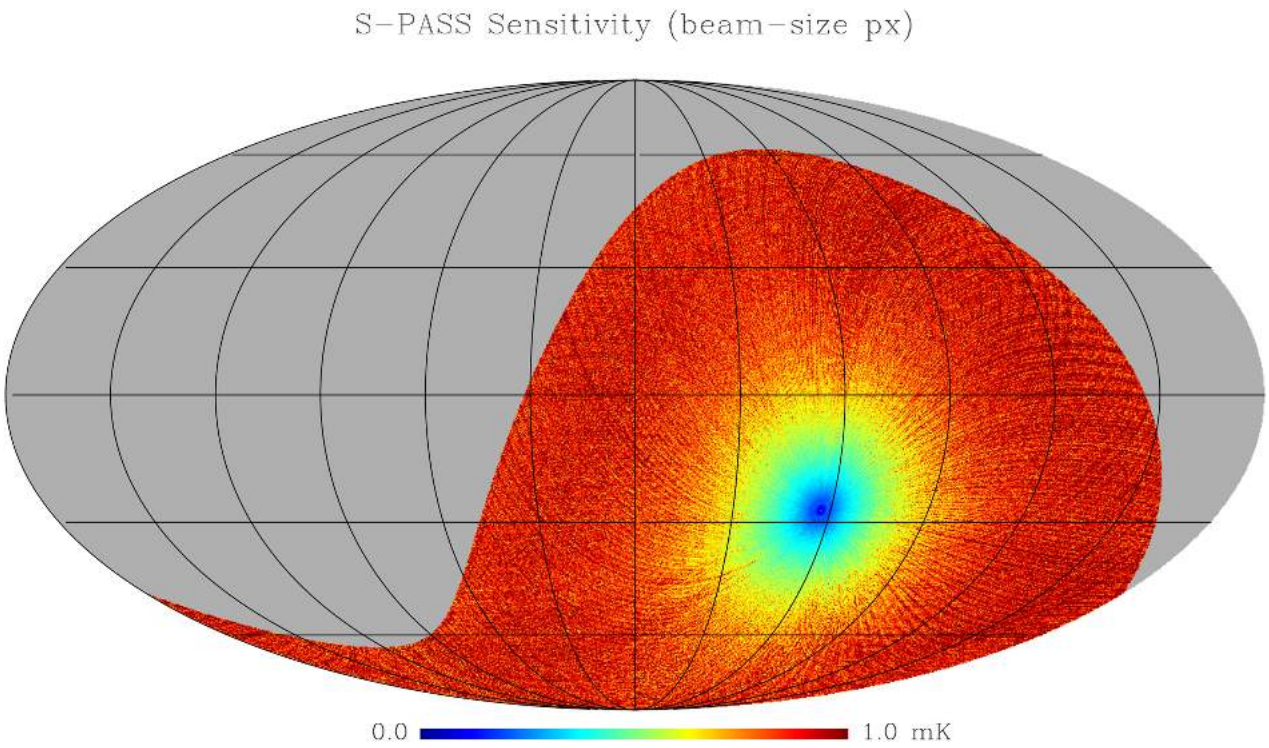

Figure 19. S-PASS sensitivity map on the beam-size scale. The map is in Mollweide projection, Galactic coordinates, with the Galactic centre at the centre and longitude increasing leftward.

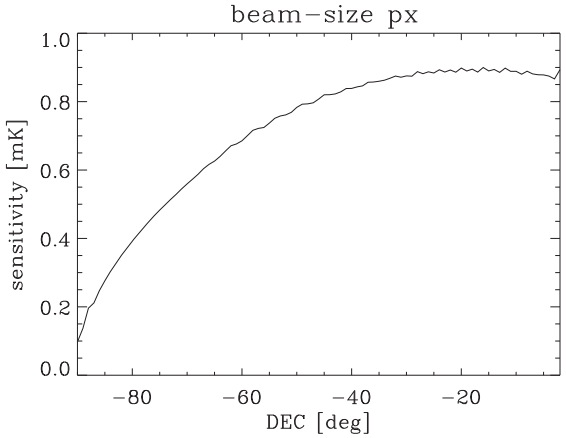

Figure 20. S-PASS sensitivity on a beam-size scale, averaged over all pixels at a given declination.

is limited by the source S/N. The mean (5.6 arcsec combined) is the systematic position error of the map. Pointing errors are therefore insignificant compared with the beam size.

The confusion limit was measured on our maps and found to be $\sigma_{I,(\mathrm{CL})} = 9$ mK (Meyers et al. 2017) at a beam resolution of 8.9 arcmin.

3 OBSERVING STRATEGY

The practical construction of an all-sky map of polarized continuum emission with a large telescope and a small beam size implies the realization of several requirements, including the following:

(i) recovering the emission at all scales, including the mean emission (offset) at the scale of the map size;
(ii) minimizing the ground-emission contamination;
(iii) scanning the sky at a fast rate and with small overheads to minimize $1/f$ noise and reduce observing time.

Recovering the mean emission is the most stringent and complicated requirement for large-scale polarization observations. Discrete object observations can make use of the background emission around the object as reference to correct and obtain the object emission. However, such reference emission does not exist for emission at very large scales (e.g. ISM diffuse emission) and it is essential to obtain a calibrated offset in order to measure emission and polarization angle correctly. An incorrect offset would result in incorrect polarization angles, compromising all the potential science based on the measurement of magnetic field direction and RM.

Subdividing the sky into smaller, square areas (e.g. $10^\circ \times 10^\circ$ or $20^\circ \times 20^\circ$ patches) and mapping them with sets of short orthogonal scans is not an option. Basket-weaving in this manner is appropriate to recover signal up to the scale of the patch size, but information on larger scales is lost.

Ground emission is usually not an issue on short scans up to a couple of degrees, where a linear baseline subtraction is usually sufficient to remove it. Moreover, the ground emission is more dependent on elevation (EL) than azimuth (AZ), one more reason to avoid standard orthogonal scans, where the scans would have an EL component.

To address all these issues, we used a scanning strategy based on fast, long azimuth scans. The scans were conducted at the elevation of the south celestial pole at Parkes (EL $= 33.0^\circ$) and were made long enough to cover all declinations from $\sim -90^\circ$ to $\sim 0^\circ$. Scans were conducted in a back-and-forth manner at a speed of 15 deg min^{-1}, with the telescope recording the position at full precision. This is a very fast rate for the Parkes telescope, being 62.5 per cent of its AZ slewing speed (24 deg min^{-1}), and required a special drive system set-up.

The Parkes telescope has an altazimuth mount and tracks the sky through the master equatorial (ME), a small equatorial mount system that easily tracks objects in celestial coordinates. The ME is equipped with a laser, the beam of which illuminates a mirror on the telescope structure and is reflected back to laser light sensors on the ME. The telescope drives are computer-operated, so that the laser beam is reflected back at the mid-point of those sensors. When this happens, the telescope is locked to the ME and the sky position is known at the precision of the ME. When the lock is lost, the telescope position is unknown and the observation aborted. This set-up does not allow scans through the south celestial pole, which is a singular point for the ME equatorial mount.

Normally, scan rates of up to some 3–4 deg min^{-1} are possible at the Parkes telescope. Faster rates tend to end up with the telescope's position tracking system losing lock soon after the scan starts, leading to observation abort. The fundamental problem here is that the rate during acceleration is too fast and the telescope cannot keep up. The drive system was thus modified to have a gentle, constant acceleration ramp-up until the nominal cruise speed was reached. The acceleration rate was 0.536 deg min^{-1} s^{-1}, with the nominal speed being reached after 28 s. Tests showed that 15 deg min^{-1} was the fastest robust rate, without occasional lock loss. Indeed, no break-lock episode occurred during the entire project. The backend also acquired data during ramp-up. The same was set for the end of the scan, with a gentle, constant deceleration ramp-down preserving full position information. Fig. 2 shows the scan rate versus AZ for a full scan. The system was not able to acquire data while ramping down.

The AZ scan range was $[61.5^\circ, 180.0^\circ]$ eastward, including the two acceleration and deceleration ramps, covering the Dec. range $[-90.0^\circ, +2.2^\circ]$. The area around the south pole was acquired during backward scans that start from the AZ $= 180.0^\circ$ end. The westward scan range was limited by the telescope's south wrap AZ limit at 294.4° spanning the range $[180.0^\circ, 294^\circ]$, covering the Dec. range $[-90.0^\circ, -0.6^\circ]$.

Earth rotation was used to cover the entire 24-h RA range. The sky rotates during each scan, so that each back-and-forth pair does not repeat the same track in the sky advancing in RA. Each night, the sky coverage was a zigzag in the sky (Fig. 3). The scans were conducted both eastward and westward when the sky rises and sets to have scans along two different directions and realize a basket-weave pattern (see Fig. 3).

With AZ scans at a fixed EL, there is no capability to scan a specific position in the sky arbitrarily at any time; rather, scans occur only once a day. Thus, to realize a regular grid in the sky, scans need to have well-defined geometry, duration and speed and start at the desired local sidereal time (LST). This makes each scan repeatable and scans can be spaced by the desired amount, even though each scan can be executed only once a day.

Each night, a sequence of back-and-forth scans was performed. To fill the sky regularly with scan sequences taken on different nights, an appropriate waiting time was left at the end of each scan, so that an integer number of back-and-forth scans fitted into 24 h of LST and the sequence of scans was a closed loop (Fig. 3). Each night, a different sequence was observed with exactly the same geometry except for an offset in RA, that is, an offset in the LST between start times. Scan separation depends on declination:

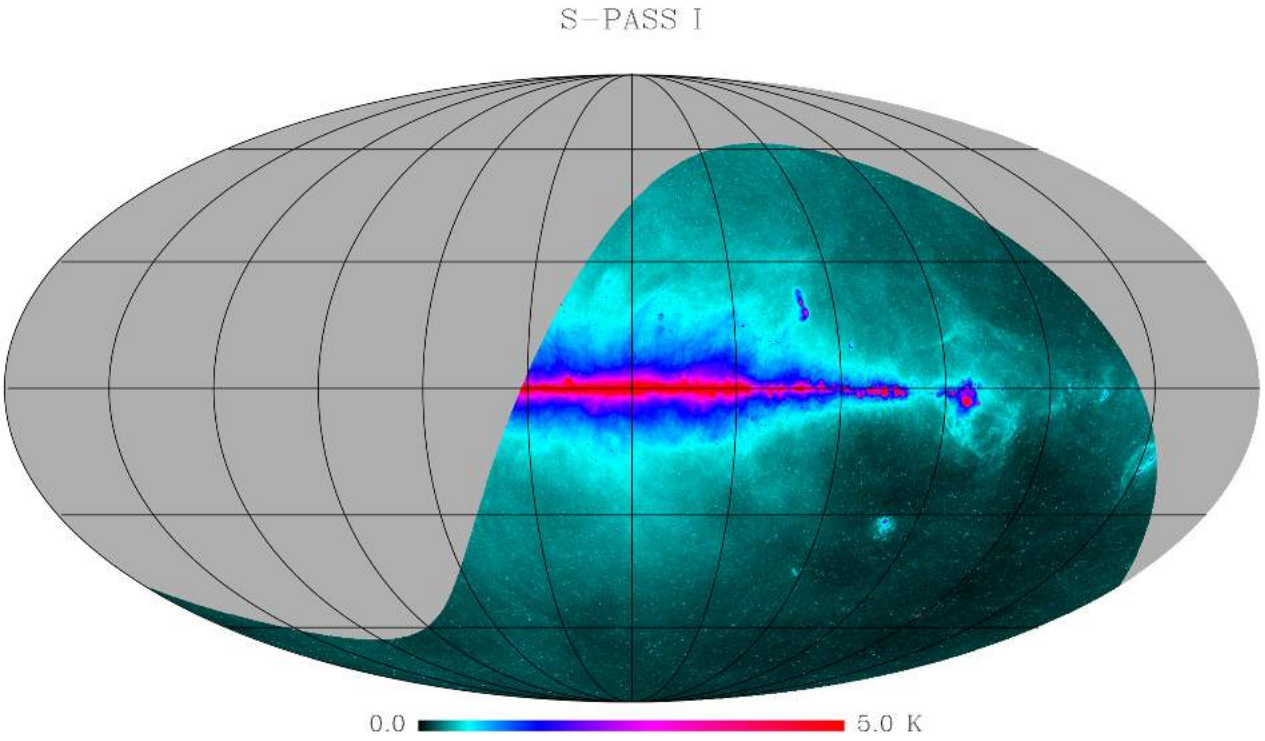

Figure 21. S-PASS Stokes *I* image. The map is in Mollweide projection, Galactic coordinates, with the Galactic centre at the centre and longitude increasing leftward.

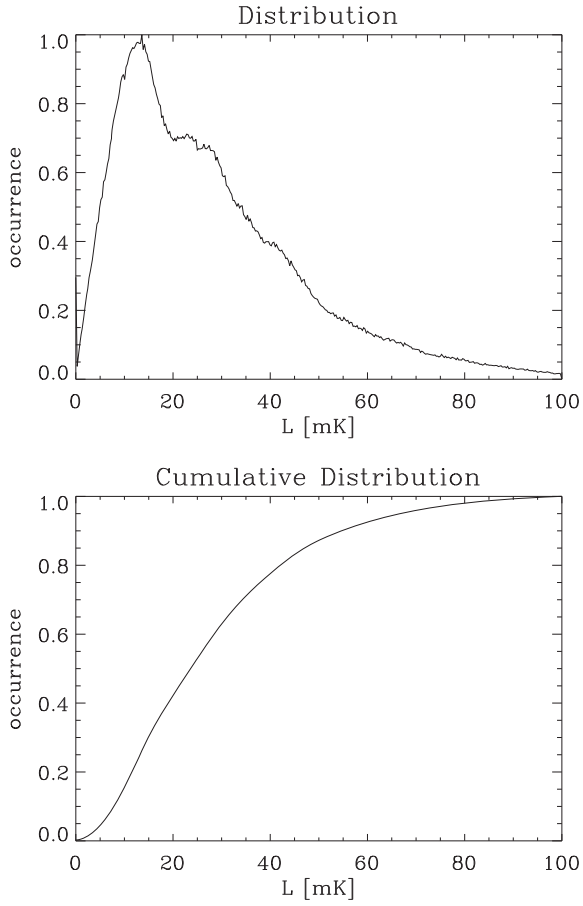

Figure 22. Distribution (top) and cumulative distribution (bottom) of the S-PASS polarized intensity *L*.

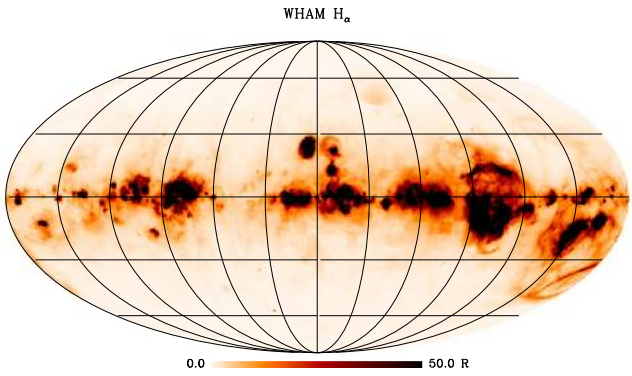

Figure 23. Hα emission as seen by the WHAM Sky Survey (Haffner et al. 2010; Haffner et al., in preparation). This map shows the total emission integrated over all spectral channels.

smallest at the south pole (all scans get there), largest at Dec. = −18.4° (Fig. 3).

For east scans, an RA/LST offset of $d_{\mathrm{RA_{east}}} = 21.6270$ s was used, for a maximum scan spacing of 4.38 arcmin at Dec. = −18.4° (Fig. 4). The maximum spacing was chosen to be smaller than half the beam size, ensuring Nyquist sampling and making all sequences equally spaced. Along with the closed loop of each zigzag sequence, this gave a regular sky coverage with all scans equally spaced. In detail, 47 zigzag sequences of 85 back-and-forth scan pairs each were observed, for a total of 3995 scans in each heading.

Since east scans alone are sufficient to sample the sky fully, west scans were performed mainly to ensure scan-crossing and basket-weaving for efficient map-making. To save observing time in this direction, we sampled the sky with a spacing of only one scan

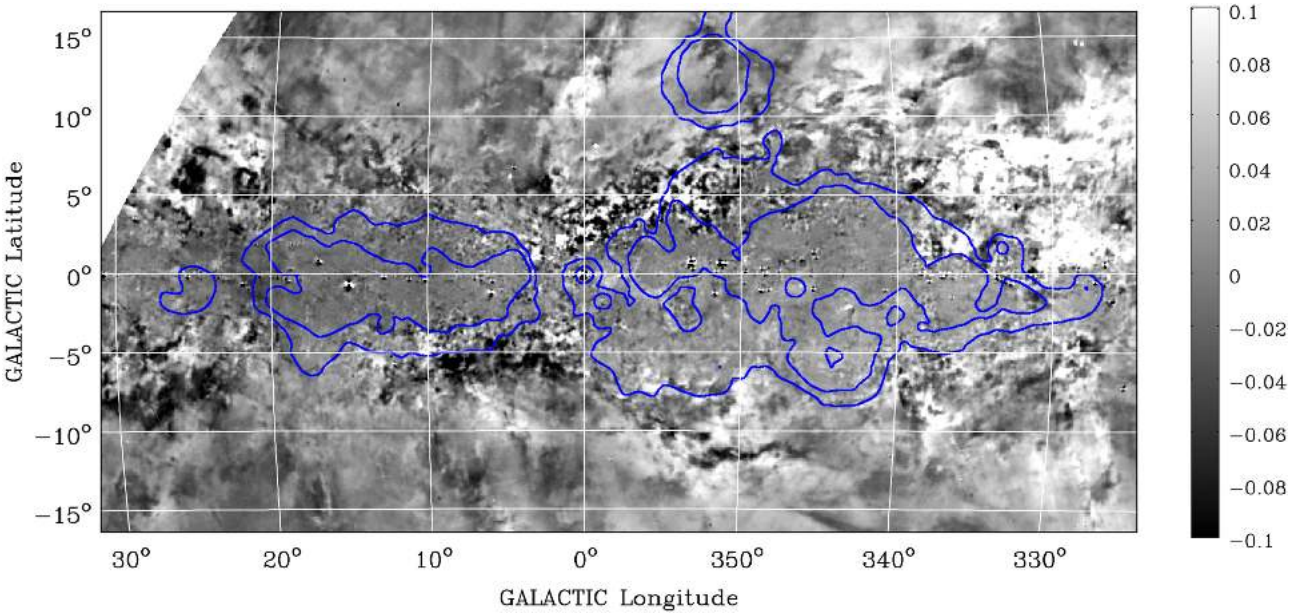

Figure 24. S-PASS Stokes Q map (colour bar units are K) with Hα emission contours from WHAM map of Fig. 23. Contours are at 22 and 44R.

per beam. The RA/LST offset between successive scans was set to $d_{\mathrm{RA_{west}}} = 42.2081$ s, for a scan spacing of 8.67 arcmin, resulting in 24 zigzag sequences of 89 back-and-forth scan pairs, for 2136 scans in each heading. Note that the number of west scans was slightly more than half the number of east scans. This was in order to realize the regular pattern described above.

Given such a scanning strategy, Solar system objects will be observed. Therefore, all data closer than 60 arcmin from the Moon and 10 arcmin from Jupiter and Mars were excluded. Considering the intensity of the first side lobe, we estimated a worst-case contamination of some 1 mK in Stokes I, negligible compared with the confusion limit and more than one order of magnitude smaller in polarization, which is negligible compared with the polarization sensitivity.

4 MAP-MAKING

4.1 Method

Basket-weaving techniques are applied to build maps and combine scans taken along crossed scans. Here we use the algorithm of Emerson & Gräve (1988). Basket-weaving, however, can recover emission only up to the size scale of the map. The baseline of each scan is usually estimated and removed and the average signal for the map area is lost.

In the context of S-PASS, this applies only to the Stokes I signal (which is not modulated during a scan). The polarized components, Stokes Q and U, are different. For these, the variation of the parallactic angle ϕ in a long azimuth scan modulates a constant polarized signal by a sinusoidal function in the instrument reference frame as

$$Q = L_0 \cos\left[2(\theta_0 + \phi)\right], \tag{3}$$

$$U = L_0 \sin\left[2(\theta_0 + \phi)\right], \tag{4}$$

where L_0 and θ_0 are the amplitude and polarization angle of a constant polarized signal. Fig. 5 shows the variation of the modulation angle 2ϕ in S-PASS east and west scans, as well as an example of how Q and U behave. The large range spanned by 2ϕ – some 90° for each east or west scan or 180° combined – introduces a large modulation of Stokes Q and U in the instrument reference frame and a baseline subtraction does not cancel a constant sky signal. Because short scans would produce little modulation, long azimuth scans are essential for this technique to be effective.

To recover the full constant signal of each scan, an unknown constant offset (in the instrument reference frame) is added to each scan, for either Stokes Q or U. This is also called destriping, because the lack of the correct offset on each scan would lead to striped maps if made by just binning the data on the same pixels. Scans cross each other at several points, where each is required to have the same sky signal. The solution is found with a maximum-likelihood procedure. The best offset parameter set is that which minimizes the sum of all the squared differences between scans at their crossing points. The least-squares criterion is justified, given the Gaussian distribution of the errors in Stokes Q and U. The system of equations to solve is reported in Appendix A.

The system to solve is computationally challenging when all scans are considered: given 12 000 scans, 24 000 unknown offsets must be solved for, requiring some two months of CPU time for each frequency channel. However, given the procedure is mainly useful in recovering the large-scale emission, it is not, in general, necessary to work at full resolution. Indeed, binning the data into a smaller number of wider scans and solving for the consequently coarser resolution map produces an adequate estimate of the large-scale emission.

After offset estimation, the Emerson & Gräve (1988) basket-weaving technique is applied. This is performed in Fourier space and requires two maps taken along two crossing directions. After solving for the offset at coarse resolution, two maps with east and west scans only are generated and combined together. The two maps are generated in equatorial coordinates using a cylindrical (Carrée) projection, which gives the rectangular-shaped images required by the technique. The technique is usually employed using straight scans, the Fourier transforms of which are straight lines, allowing simple and effective Fourier filtering. However, our

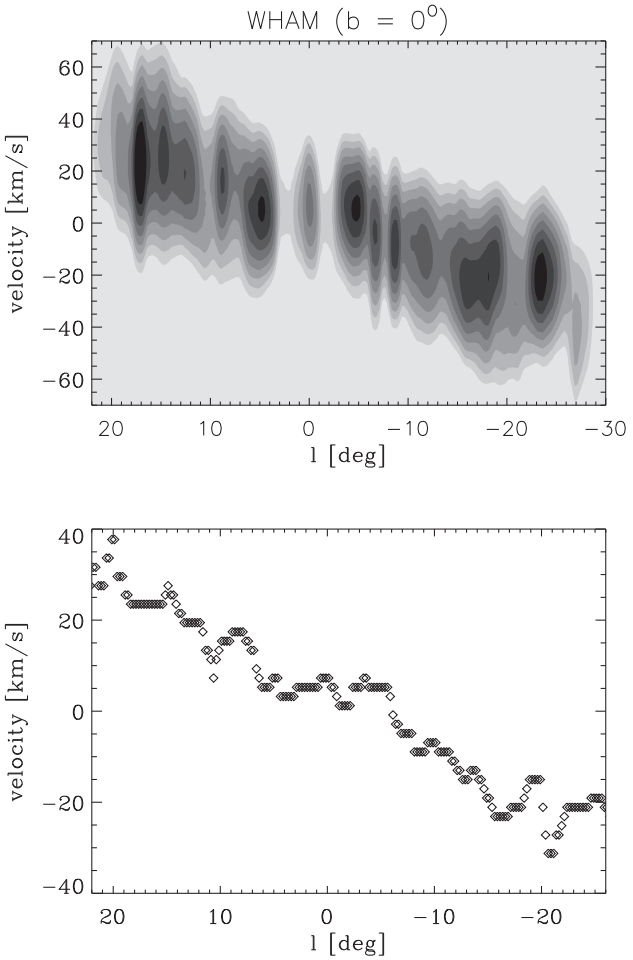

Figure 25. *Top:* position–velocity (radial velocity in the kinematic local standard of rest – LSRK – system) map of the Hα emission of the two large regions in the central part of the inner Galaxy (Galactic longitude $l \sim [20°, -30°]$) from the WHAM Sky Survey (Haffner et al. 2010, Haffner et al., in preparation) for a latitude slice centred on $b = 0°$, of width $\Delta b = 1°$. Contours start at $1R$ (km s^{-1}) and scale by a factor of $\sqrt{2}$ each. *Bottom:* for the same slice, the velocity where the emission peaks at each longitude bin is plotted versus Galactic longitude.

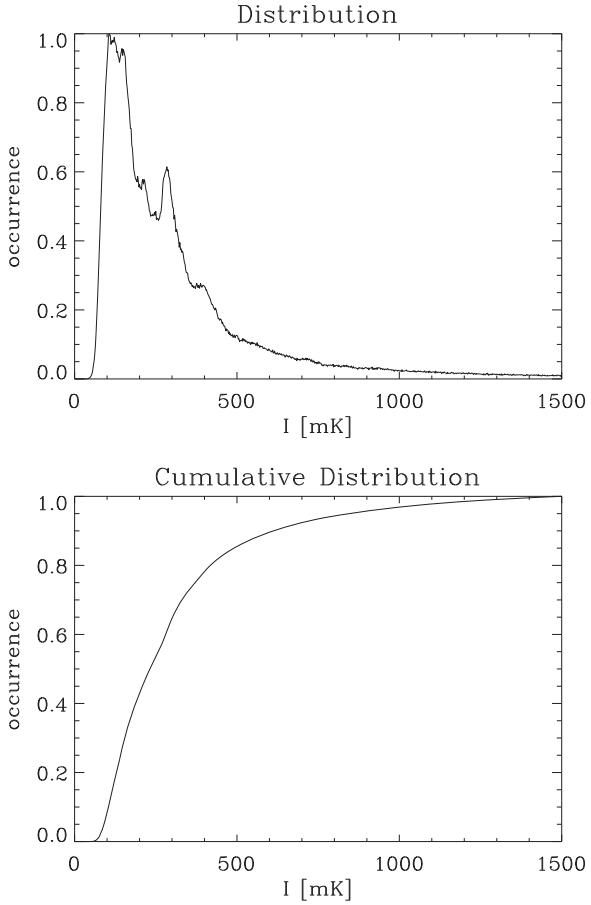

Figure 26. Distribution (top) and cumulative distribution (bottom) of the S-PASS total intensity *I*.

scans are not straight lines. Their Fourier-space images are quite complex and spread over almost the entire Fourier space, making it harder to set up dedicated filters. East and west scans were therefore approximated with linear fits to set the Emerson and Gräve Fourier filters. The coarse-resolution maps so obtained were then converted to Galactic coordinates.

The final, full-resolution map is then generated using the coarse-resolution, absolutely calibrated map from which the correct baseline for each scan can be determined. The baseline is obtained using a running median of the difference between each scan and the absolutely calibrated map. Once corrected, the data from the original scans are binned in the final map at full resolution. The polarization vectors were all parallel-transported to the centres of the nearest map pixel, in order to avoid false depolarization due to the variation of the reference direction across each pixel. The effect increases with decreasing distance to the pole. We apply this to all pixels, regardless of their distance from the pole. The HEALPIX pixelation (Górski et al. 2005) in Galactic coordinates was used with parameter *nside* = 1024, corresponding to pixels of $\theta_{\rm px} =$ 3.4 arcmin, which ensures adequate sampling of the beam. HEALPIX pixels are equal-area and isolatitude.

In summary, the steps of the procedure to obtain the final maps at full resolution are as follows (see also the diagram of Fig. 6).

(i) Scans are binned into 0.5° wide scans. Data are also binned along a scan to 0.5° pixels.

(ii) The equation system determining the optimal set of offset values is solved (Appendix A) for these coarse resolution scans.

(iii) Offset-corrected scans are used to generate two maps generated from data taken in different scan directions, i.e. east and west.

(iv) East and west maps are combined with the technique of Emerson & Gräve (1988), which gives the final zero-offset calibrated map at coarse resolution.

(v) The baseline for each original scan is corrected by matching to the coarse-resolution zero-offset calibrated map.

(vi) The final maps at full resolution are obtained from the offset-corrected scans binned using a HEALPIX projection with a pixel size of 3.4 arcmin (*nside* = 1024).

Stokes *I* maps are obtained in a similar manner, with the equations to estimate the scan offsets defined in Appendix B. However, the map-making procedure and scanning strategy were optimized for *Q* and *U* only. Stokes *I* is not modulated, so the output map has the overall mean value undetermined.

Instead, this is recovered using archival, absolutely calibrated observations of the south celestial pole (SCP) taken at 2.0 GHz

by Bersanelli et al. (1994) with a horn radiometer of $\mathrm{FWHM_h} = 22^\circ$ at the South Pole Station pointing to the zenith. These authors measured a Galactic component of

$$T_{2.0}^{\mathrm{SCP},22^\circ} = 325 \pm 100\,\mathrm{mK}. \quad (5)$$

Scaling with a brightness temperature spectral index of $\beta = -2.7$ and assuming a spectral index uncertainty of $\sigma_\beta = 0.2$ ($1-\sigma$), we obtain an estimate of the emission at 2.3 GHz of

$$T_{2.3}^{\mathrm{SCP},22^\circ} = 220 \pm 70\,\mathrm{mK}, \quad (6)$$

including measurement and spectral index errors.

The Stokes *I* map obtained with the map-making procedure is smoothed to $\mathrm{FWHM_h} = 22^\circ$ and the difference between the value of equation (6) and that of the smoothed map at Dec. $= -90^\circ$ is then added to the unsmoothed map to offset it appropriately. This delivers a Stokes *I* map absolutely calibrated for Galactic emission. (Note that CMB emission has not been included.) Proceeding this way, the error of 70 mK applies to the mean level only. For all other scales, the error is smaller and dominated by the statistical noise or the confusion limit (9 mK).

4.2 Tests: *Q* and *U*

To test the map-making procedure, we performed a simulation with realistic input *Q* and *U* maps. Observed scans were extracted from the input maps and Gaussian noise added to each sample with the same rms as observed (assuming the noise measured for the entire useful band). The baseline was then subtracted from each scan to mimic the process in a normal data reduction and then the entire map-making procedure was applied. The baseline-removing procedure excludes strong compact sources and areas with strong diffuse emission to avoid strong deviations of individual scans. Baseline removal was performed by an automatic procedure that runs the baseline-fitting once, flags outliers and then repeats the fit. This was repeated a few times with decreasing outlier threshold to ensure that only the strongest sources were flagged in first iteration, with the threshold progressively being refined to flag weaker compact sources.

The output maps were then compared with the input ones to assess how well the process was reconstructed. We used the same HEALPIX pixelation as for the S-PASS maps.

For input maps for the simulation, we used the *WMAP* polarization maps at 23 GHz (Bennett et al. 2013), which contain emission that is mostly Galactic synchrotron. For a realistic signal level, the 23-GHz amplitude was scaled to 2.3 GHz with a brightness temperature spectral index of $\beta_{\mathrm{scal}} = -3.2$, the typical slope at high Galactic latitudes (Carretti et al. 2010). Mid and low Galactic latitudes have flatter indexes, ensuring the map presents a worst-case scenario.

Faraday depolarization is insignificant even on the Galactic plane at 23 GHz, so the *WMAP* sky reveals strong disc emission in the inner Galaxy. As we will see later, the emission at 2.3 GHz is strongly depolarized there, making the signal much weaker. To account for this, we apodized the *WMAP* map in the Galactic plane with a Hanning filter of 15° width. This effectively weakens the signal within a few degrees around the Galactic plane, mimicking a more realistic measurement. The resulting maps are shown in Fig. 7, top panels.

The mean signal in the input maps is $\overline{Q}_{\mathrm{WMAP}} = 8.8$ mK and $\overline{U}_{\mathrm{WMAP}} = -3.2$ mK for Stokes *Q* and *U*, respectively. These are the mean signals (or offsets) that the map-making procedure must be able to reconstruct to recover the absolutely calibrated signal. Since *Q* and *U* are signed quantities, the mean measures the offset, but does not measure the typical intensity of the signal. This can be measured by the rms values $Q_{\mathrm{rms,\,WMAP}} = 24$ mK and $U_{\mathrm{rms,\,WMAP}} = 29$ mK, or by the mean polarized intensity $\overline{L}_{\mathrm{WMAP}} = 28$ mK.

Simulated observational data were generated as described above and then the map-making procedure was applied. The output maps (Fig. 7, bottom panels) are nearly identical to the input ones. We find that the rms of the difference between the two maps is 2.26 mK on pixel scales (3.4 arcmin) and 0.81 mK on beam-size scales (FWHM = 8.9 arcmin), consistent with the expectation from instrumental noise alone. The error from the map-making procedure is thus not adding significantly to the error budget.

The mean values of the difference maps measure how well the mean values of the input maps are recovered (i.e. the zero-offset calibration). We find that they are $\overline{\Delta Q}_{\mathrm{WMAP}} = 0.021$ mK and $\overline{\Delta U}_{\mathrm{WMAP}} = 0.017$ mK, consistent with zero within 2σ (the error in the mean with our instrumental noise is 0.010 mK). The mean emission (offset) is then recovered with a precision better than 1 per cent (0.24 per cent and 0.53 per cent for Stokes *Q* and *U*, respectively). The map-making procedure thus recovers the input maps correctly. Indeed, even the mean emission is recovered with high precision.

To estimate the error contributed by the map-making procedure alone, a simulation with no noise was also made. The output maps are essentially identical. The histograms of the differences between output and input maps are shown in Fig. 8. The distribution is symmetric at the centre, but shows some asymmetry in the wings. The 16 and 84 per cent cumulative distribution limits are (−0.18, +0.17) mK and (−0.21, +0.10) mK for *Q* and *U*, respectively. The uncertainty in the map-making procedure is thus much smaller than both the typical signal in the maps (by three orders of magnitude) and the pixel noise (by more than a factor of 10), further confirming that its contribution to the error budget is negligible.

The mean values of the differences are 0.023 and 0.012 mK for *Q* and *U*, similar to the case with instrumental noise included. Fractional errors are 0.26 and 0.38 per cent.

For very faint emission regions, Fig. 9 shows the distribution of the differences only for pixels with $L < 10$ mK. This distribution is more symmetric and approximately half as wide as the general case, with 16 and 84 per cent cumulative distribution limits of (−0.09, +0.09) and (−0.12, +0.10) mK for *Q* and *U*, respectively.

All the above indicate excellent performance. In the observational noise case, the error distribution is consistent with the instrumental noise, with negligible contribution from the map-making procedure. The no-noise case suggests that the analysis error is approximately 0.1 mK in low-emission regions where $L <$ 10 mK, 23 times weaker than the pixel sensitivity and eight times better than the sensitivity in beam-sized areas. In higher emission areas, the error is a bit larger in absolute terms at some 0.2 mK, but in relative terms it is negligible, with signal-to-noise ratio S/N > 50.

4.3 Tests: Stokes *I*

The Stokes *I* map-making procedure was tested in a similar manner, with the major difference being that the input map is more complicated, because the total intensity emission is a combination of several components, including synchrotron, free–free and CMB. We used the Planck Sky Model (Delabrouille et al. 2013) computed at 2.3 GHz, which uses several data sets from radio to millimetre wavelengths to scale the relevant components in frequency appro-

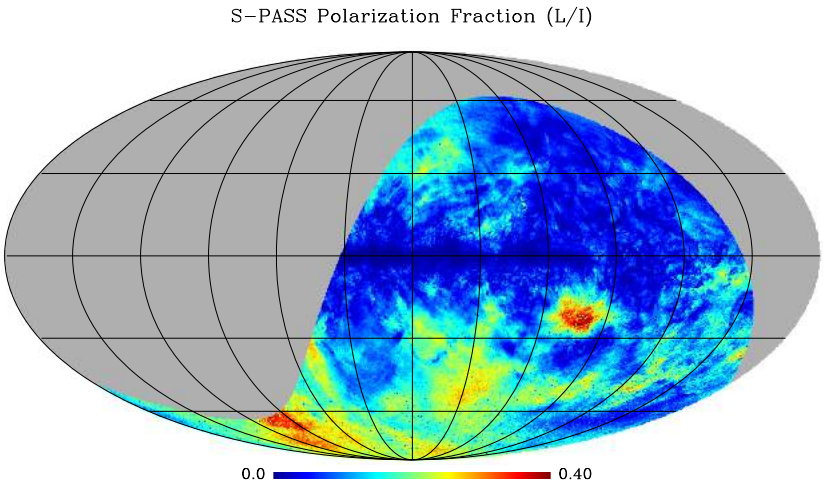

Figure 27. Fractional polarization *L*/*I* from S-PASS.

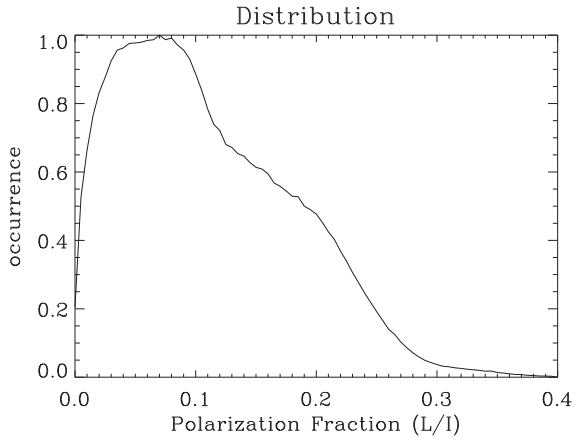

Figure 28. Distribution of the fractional polarization *L*/*I*.

priately. The input map we used is shown in Fig. 10. The mean signal is $\overline{I}_{\rm PSM} = 155$ mK and the weakest emission $I_{\rm PSM,\,min} = 24$ mK.

Simulated data were generated as described in Section 4.2, then the map-making procedure was applied. Some of the mean emission is lost as expected and the output map is offset by $\Delta I = -99.6$ mK. Setting this aside, Fig. 10 shows that the two maps are nearly identical. The rms of their difference is 2.7 mK, slightly larger that one would expect from the instrumental noise, evidence that, in this case, the map-making procedure adds a non-negligible contribution.

To verify this, the no-noise case is shown in Fig. 11. The rms is 1.5 mK, with some asymmetry, with 16 and 84 per cent cumulative distribution limits at $(-1.6, +1.4)$ mK. The map-making procedure error is thus smaller than, but comparable with, the expected statistical error (2.26 mK) and accounts for the larger total rms we obtain in the instrumental noise case.

This, however, has a minor impact on our maps. First, the error budget is dominated by the confusion limit (9 mK) and the map-making procedure contribution to the total rms is negligible at ∼1 per cent. Then, compared with the sky signal, the map-making error ensures $S/N > 15$ everywhere in the sky and an ample $S/N > 100$ compared with the mean signal. The map-making procedure thus reconstructs the input map with negligible error compared with the sky signal.

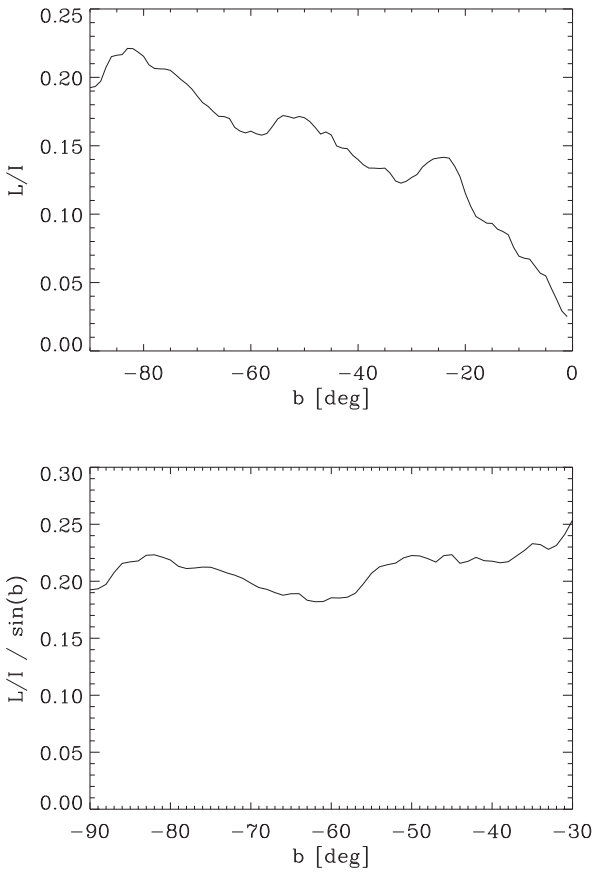

Figure 29. Average fractional polarization *L*/*I* (top) and corrected for sin *b* (bottom) versus Galactic latitude *b*. The latter is expected to be constant in the case in which the local emission below the Galactic plane has a polarization angle parallel to the Galactic plane.

5 GROUND EMISSION

Ground emission is estimated and cleaned from low-emission areas, after the data are calibrated and before the map-making procedure is applied. For each set of azimuth scans – east or west – all points at the same declination share the same ground-emission contamination. Following Wolleben et al. (2006) and Carretti et al. (2010), all data

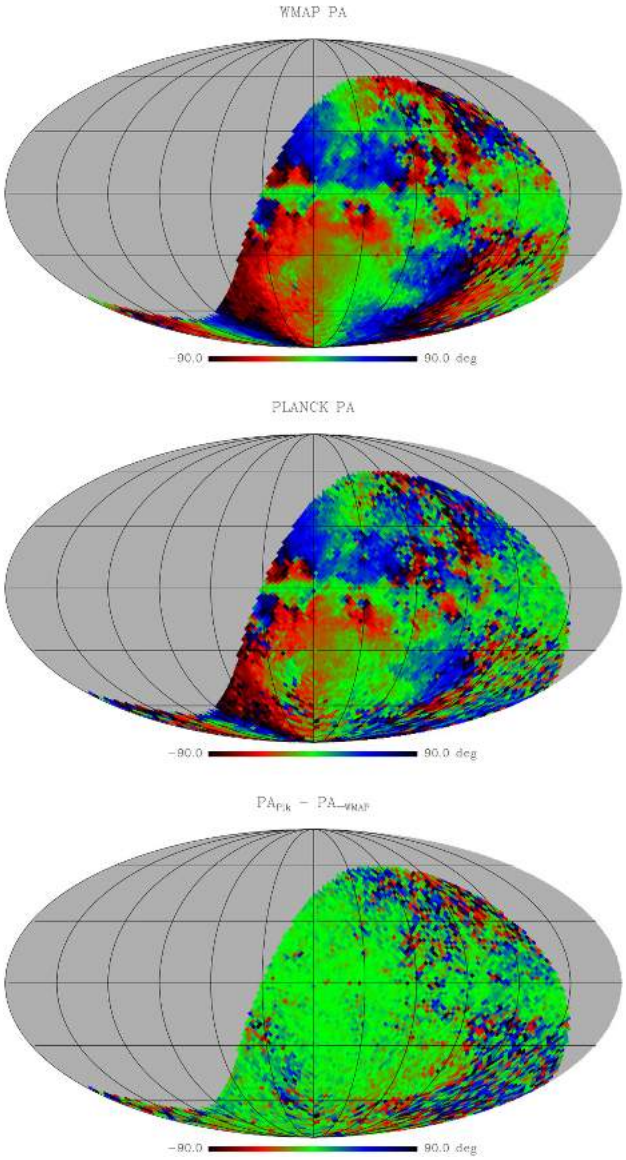

Figure 30. *WMAP* polarization angle map at 23 GHz (top), *Planck* map at 30 GHz (middle) and their difference (bottom).

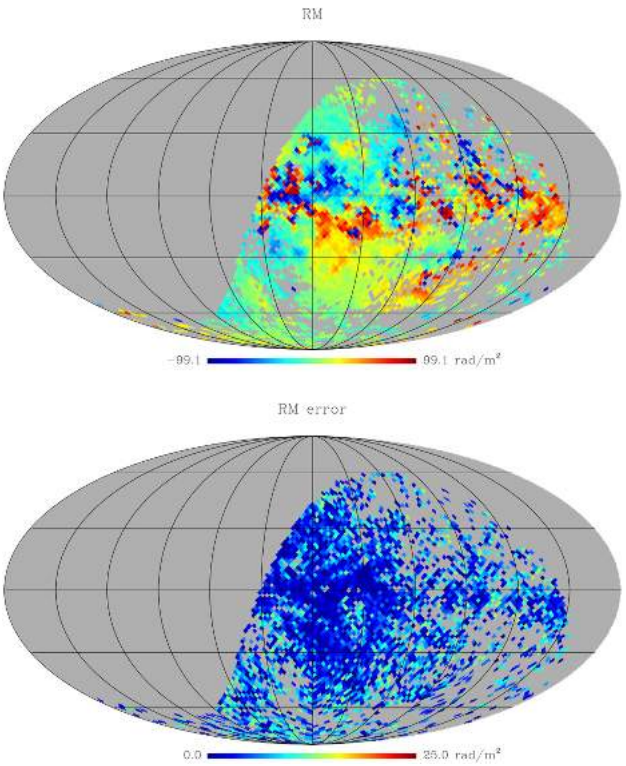

Figure 31. Top: map of RM obtained combining best-fitting S-PASS (2.3 GHz), *WMAP* (22.8 GHz) and *Planck* (28.4 GHz) polarization angle maps. Bottom: RM errors ($1-\sigma$) from the fit procedure.

taken in low-emission areas are averaged. Stokes Q and U change sign, which makes the averaged sky component tend to zero, and the final average value gives a reliable estimate of the ground emission.

It is worth noting an important caveat that affects all surveys where the ground emission is estimated this way: because the estimate is carried out in constant-declination rings, the average sky emission at the same declination will be subtracted and any average declination dependence will be subtracted with the ground. This residual cannot be estimated precisely (it would require an a priori knowledge of the actual sky emission); however, a few considerations suggest that it is small. In addition to the points listed above, sky emission is mainly a function of Galactic coordinates, rather than declination. This makes the residual subtracted term tend to zero. A constant component of the signal in Galactic coordinates produces a full modulation in polarization angle along a declination ring, so its average would approach zero. The signal components on smaller angular scales also have an average that tends to zero. Overall, the residual subtracted signal will be small compared with the typical signal even in low-emission areas.

We selected low-emission areas using *WMAP* maps as a guide. After cleaning, these were confirmed by the final S-PASS maps themselves, with the only addition to the mask being the region centred approximately at $l = 290^\circ$, $b = -20^\circ$, as shown in Fig. 12.

Fig. 13 shows the ground-emission profile for Stokes Q and U. The ground component is about an order of magnitude lower than was measured by Wolleben et al. (2006), proving the benefit of the AZ scan-based strategy. These ground-emission profiles are subsequently subtracted from the AZ scans.

Were there errors in such a procedure, they would leave residual ground emission that, because of the scanning strategy, would appear as rings concentric to the south Celestial pole. As we will see in the next section, the maps we obtain have no obvious signs of such structures, even where the signal is low, a sign that residual contamination is negligible compared with the sky signal.

To obtain a more quantitative estimate of the possible residual contamination, we have compared cleaned east and west scans at the same declination. Ground emission for these two sets of scans is different and independent, while the average sky emission at the same declination is the same (but see later), so any difference between the two could only be due to residual ground emission. In particular, west scans at azimuth $(360^\circ - \mathrm{AZ})$ share the same Dec. as east scans at azimuth AZ. Thus, an estimate of possible residual ground contamination can be obtained from

$$\Delta X = \frac{X_\mathrm{w}(360^\circ - \mathrm{AZ}) - X_\mathrm{e}(\mathrm{AZ})}{2} \qquad \text{where } X = Q, U, L \qquad (7)$$

Table 3. Scientific journal articles based on S-PASS data published to date.

	Title	Topic	Reference
1	Giant magnetized outflows from the centre of the Milky Way	Discovery of the Milky Way's giant radio lobes, the polarized radio counterparts of the γ-ray Fermi bubbles	Carretti et al. (2013a)
2	Detection of a radio bridge in Abell 3667	Discovery of ICM extended emission connecting the cluster centre to outer relics	Carretti et al. (2013b)
3	Absolutely calibrated radio polarimetry of the inner Galaxy at 2.3 and 4.8 GHz	Analysis of the magnetic properties of inner Galaxy spiral arms	Sun et al. (2014)
4	Galactic interstellar turbulence across the southern sky seen through spatial gradients of the polarization vector	First ISM turbulence map on an all-sky size scale	Iacobelli et al. (2014)
5	A radio-polarization and rotation measure Study of the Gum Nebula and its environment	Study of the nature of the Gum Nebula	Purcell et al. (2015)
6	Magnetic field disorder and Faraday effects on the polarization of extragalactic radio sources	Fractional polarization behaviour with frequency and other parameters of the S-PASS compact source bright sample	Lamee et al. (2016)
7	A southern-sky total intensity source Catalogue at 2.3 GHz from S-band Polarization all-sky survey data	Compact source catalogue of S-PASS (Stokes *I* only)	Meyers et al. (2017)
8	A new perspective on turbulent Galactic magnetic fields through comparison of linear polarization decomposition techniques	ISM turbulence analysis tools with multi-scale wavelets and E/B-mode decompositions	Robitaille et al. (2017)
9	Limiting magnetic fields in the Cosmic Web with diffuse radio emission	New upper limits on the Cosmic Web synchrotron emission and magnetic field intensity	Brown et al. (2017)
10	Advanced diagnostics for the study of linearly polarized emission. II. Application to diffuse interstellar radio synchrotron emission	New diagnostic tools to study diffuse linear polarized emission	Herron et al. (2018)
11	The jet/wind outflow in Centaurus A: a local laboratory for AGN feedback	New findings in Cen A lobes/outflows	McKinley et al. (2018)
12	Ghost of a shell: magnetic fields of Galactic supershell GSH 006–15+7	Magnetic field analysis of a Galactic supershell	Thomson et al. (2018)
13	Interstellar magnetic cannon targeting the Galactic halo: a young bubble at the origin of the Ophiuchus and Lupus molecular complexes	Discovery of a new, large, local cavity in the inner Galaxy and its dynamic analysis	Robitaille et al. (2018)
14	The S-PASS view of polarized Galactic synchrotron at 2.3 GHz as a contaminant to CMB observations	High precision analysis of Galactic polarized synchrotron emission as a CMB foreground over the entire southern sky	Krachmalnicoff et al. (2018)
15	S-PASS/ATCA: a window on the magnetic universe in the southern hemisphere	Compact-source RM catalogue of the S-PASS sample followed up with broad-band ATCA observations	Schnitzeler et al. (2019)
16	S-band Polarization All Sky Survey (S-PASS): survey description and maps	S-PASS survey description article	This article

and e and w denote east and west scans. In reality, even if the declination is the same, the parallactic angle differs in general between two points. This means that the sky emission is not identical, but mixed between Q and U depending on the difference in parallactic angle. The quantity in equation (7) thus accounts for any additional difference due to the sky for Q and U and represents a worst case of the ground residual leftover. To ameliorate any such effect, we only use data for which the polarized emission is lower than 20 mK; this corresponds to about 50 per cent of the sky covered by S-PASS and allows all azimuths to be checked. Note that the linear polarization $L = \sqrt{Q^2 + U^2}$ is not affected by the PA rotation issue and represents a more accurate estimate of the residual ground contamination.

Fig. 14 shows the residual contamination and Table 2 reports the rms values. The rms of the ground residual for linear polarization L is $\sigma_{g,L} = 0.35$ mK, which we hereafter quote as the ground emission residual contribution to the error budget of our maps.

Stokes I does not average to zero, but an approach similar to that for Q and U measurement was used in our analysis. In particular, we averaged the data taken in low-emission areas in azimuth bins that share the same ground emission. This means the mean signal emission in low-emission areas is removed, but this is not an issue, because the mean level is lost in any case. Fig. 15 shows the ground-emission profile estimated this way. Residual emission is estimated as for Q and U, as the semi-difference between the mean emission of east and west scans after the data are cleaned:

$$\Delta I = \frac{I_{\rm w}(360^\circ - {\rm AZ}) - I_{\rm e}({\rm AZ})}{2}. \quad (8)$$

Fig. 16 plots the residual error as a function of AZ; its rms value is $\sigma_{g,I} = 4.3$ mK (Table 2).

6 MAPS

The map-making procedure explained above was applied to the observed data. Polarization maps are shown in Figs 17 (Stokes Q and U) and 18 (polarized intensity L). All maps are in brightness temperature T_b units. These images have been rebinned to *nside* = 512 (pixels of 6.8 arcmin) to give a better idea of the data quality and sensitivity on a beam-size scale. The polarized intensity has been debiased using (e.g. Wardle & Kronberg 1974)

$$L = \sqrt{Q^2 + U^2 - \sigma_{\rm px}^2}, \tag{9}$$

where $\sigma_{\rm px}$ is the pixel sensitivity.

Fig. 19 shows the map of the sensitivity for beam-size pixels ($1-\sigma$) and Fig. 20 the sensitivity profile versus declination, where the sensitivity is averaged over all pixels at the same declination. The mean sensitivity is $\sigma_b = 0.81$ mK; it is worst at Dec. $=-18.4^\circ$ ($\sigma_{\rm max} = 0.89$ mK), where the scan spacing is largest, and is best ($\sigma_{\rm SCP} = 0.1$ mK) at the South Celestial Pole, where all scans converge.

The S-PASS Stokes I map shown in Fig. 21 incorporates the mean offset calibration described in Section 4. The rms fluctuations are dominated by the confusion limit $\sigma_{I,({\rm CL})} = 9$ mK. This dominates the error budget compared with all other terms – i.e. map-making residual, ground emission residual and instrument noise.

6.1 Signal statistics and map description

The polarized signal distribution is shown by the histogram and cumulative distribution in Fig. 22. The mean emission is $\bar{L} = 29$ mK.

At the low-emission end there is a peak at $L \sim 13$ mK, which can be regarded as the typical emission in the low-emission areas and a reference to use by any experiment dealing with Galactic synchrotron emission as a foreground contaminant (e.g. CMB experiments).

For stronger polarized emission regions, there is a flat plateau spanning 20–30 mK, followed by a slow roll-off to high emission.

From the cumulative distribution we find that 98.6 per cent of the S-PASS area has a signal-to-noise ratio $S/N > 3$ and that 50 per cent of the S-PASS sky is fainter than 23.6 mK.

The Q and U maps show that much of the depolarization screen seen at a lower frequency of $|b| < 30^\circ$ is lifted at 2.3 GHz, and signal is visible well below that edge. Smooth and extended structures, evidence of little Faraday depolarization or modulation, stretch almost down to the Galactic plane, with only a few degrees across the plane still modulated by Faraday rotation or depolarized. The largest depolarization regions are in the inner Galaxy on either side of the Galactic plane, reaching up to $|b| \sim 10^\circ$. At all other longitudes, signs of strong depolarization or FR are limited to lower latitudes, except for a few individual regions. e.g. the Gum Nebula or ζ Oph at $(l, b) \sim (5^\circ, 25^\circ)$.

Extended and smooth structures are visible in the maps. The most striking feature stretches from the south Galactic cap at around $l = 330^\circ - 360^\circ$, $b = -60^\circ$ to the northernmost end of the S-PASS area, a length of 100° or more. These structures are the radio polarization counterparts of the γ-ray Fermi bubbles (Carretti et al. 2013a; Su, Slatyer & Finkbeiner 2010) emanating from the Galactic Centre.

The two central depolarization regions at $l \sim [0^\circ, 20^\circ]$ and $l \sim [335^\circ, 360^\circ]$, respectively, closely correspond to two large areas of Hα emission as seen in the WHAM Sky Survey[2] in Fig. 23 (Haffner et al. 2010; Haffner et al., in preparation). Hα is a tracer of the ionized medium that, combined with the magnetic field, generates FR and related effects. Fig. 24 shows the contours of two Hα ISM clouds overlaid with Stokes Q emission and shows there is an excellent correlation between the cloud edges and the S-PASS areas where the signal is depolarized or heavily FR modulated. We show Stokes Q because we deem it better suited than the polarized intensity L for showing areas of heavy FR modulation, which generate variations of the polarization angle that L cannot capture. Stokes U, not shown here, gives similar results. The position-velocity plot of the two clouds (Fig. 25) reveals that the velocity changes linearly from 30 km s^{-1} at $l \sim 20^\circ$ to -30 km s^{-1} at $l \sim 340^\circ$, consistent with the kinematics of a spiral arm at a distance from the Sun of 2 kpc (e.g. see Dickey 2013) that matches the Sagittarius arm, midway between our location and the Galactic bulge.

Frequency spectral index behaviour is studied by Krachmalnicoff et al. (2018) who, comparing S-PASS, *WMAP* and *Planck* maps, find that the distribution peaks at $\hat{\beta} = -3.2$ with an rms spread $\sigma_\beta \sim 0.2$. The same authors also studied the spatial behaviour via polarized angular power spectra (APS). Besides the global spectra at different Galactic latitude cuts, they also computed it in ∼400 deg^2 areas (1 per cent of the sky each), showing the best sky spots for CMB investigations.

At mid and high Galactic latitudes, where Faraday rotation is negligible, S-PASS maps are an excellent match to higher frequency data, with no decorrelation within the noise limits (Krachmalnicoff et al. 2018). This shows that not only is depolarization negligible, but Faraday rotation is small, making maps at this frequency an excellent data set to study foreground contamination in CMB experiments. Krachmalnicoff et al. (2018) also use S-PASS to characterize polarized Galactic synchrotron emission with unprecedented sensitivity.

Fig. 26 shows the distribution and cumulative distribution of Stokes I. The mean emission is $\bar{I} = 420$ mK, with 50 per cent of the pixels with emission lower than 230 mK. At the low-emission end there is a broad peak, broadly spanning the range 90–180 mK, that can be regarded as the typical emission range in the low-emission areas of the map.

Fig. 27 shows the map of polarization fraction L/I, with the distribution of pixel values shown in Fig. 28. An asymmetry is observed, with the southern hemisphere generally showing higher polarization fraction. The polarization fraction in the Galactic plane is close to zero, with the lowest spots corresponding approximately to Milky Way spiral arm locations. This is due to three effects: (1) the synchrotron emission in the Galactic plane being mixed with unpolarized free–free emission, leading to a lower total polarization fraction; (2) the tangled magnetic field through the thick spiral ams leading to line-of-sight depolarization, a pure geometrical effect independent of the frequency; (3) higher free electron column density, which leads to higher Faraday rotation and in turn depolarization, in the plane and at spiral arm locations. The north–south asymmetry might be related to Stokes I emission from the Local Arm and the Gould Belt that is offset to northern Galactic latitudes in most of the area covered by S-PASS, in particular in the inner Galaxy, as also appears clear from the S-PASS Stokes I map.

The South Galactic Cap typically has high polarization fractions, from 25–40 per cent. This is not that far from the maximum for

[2]Maps available at http://www.astro.wisc.edu/wham-site/wham-sky-survey/wham-ss/

synchrotron emission and might be evidence that the local, off-the-plane magnetic field (below the Galactic plane at the Solar location) is mostly parallel to the Galactic disc with little vertical component. In such a case, L/I should behave as $(L/I)\sin(|b|)$ at high latitudes, on average. This is supported by Fig. 29, where (L/I) corrected for $\sin(|b|)$ is approximately constant versus b from the south Galactic pole down to $b \sim -40^\circ$. This is consistent with the small vertical component of the local, off-the-plane magnetic field found with RM analysis of the South Galactic Cap (Mao et al. 2010).

The polarization fraction distribution peaks in the range 2–10 per cent, but values up to 20–30 per cent are quite common and polarization fractions up to 40 per cent can be observed.

6.2 Rotation measure

We combined S-PASS polarization maps with *WMAP* (Bennett et al. 2013) and *Planck* (Planck Collaboration 2018) archival polarization data at 23 and 30 GHz, respectively – we assumed their nominal frequencies, 22.8 and 28.4 GHz, respectively. However, because of the low signal at high frequencies, there are regions where meaningful RM measurements cannot be obtained. To select the most reliable areas for RM measurement, we compare the polarization angles in Fig. 30, which shows *WMAP* and *Planck* polarization angle maps and their difference in the area covered by S-PASS. To increase sensitivity, the data were binned in pixels of 2° ($nside = 32$). While the two maps generally match well, there are areas with large differences that can exceed 30–40°, up to 90°. All these areas have low polarized emission.

These differences cannot be attributed to Faraday rotation. A difference of 45° between 22.8 and 28.4 GHz would mean a RM of 12 760 rad m^{-2}, far too high for those latitudes, where values of the order of 10–20 rad m^{-2} or less are measured by other tracers at high latitudes (e.g. extragalactic sources at high latitudes (Oppermann et al. 2015) or in the south Galactic cap (Mao et al. 2010)).

Instead, the differences are possibly residual errors in either or both maps, perhaps due to residual zero-offset calibration errors that, in low-emission regions, turn into large errors in polarization angle. Regardless of their origin, and given we cannot discern which of the two maps is most affected, we exclude from our analysis all pixels where the *WMAP–Planck* angle difference exceeds 15°.

For all other pixels, RM is computed by a best-fit procedure to the S-PASS, *WMAP* and *Planck* data using the linear relation

$$\phi_\lambda = \mathrm{RM}\,\lambda^2 + \phi_0, \tag{10}$$

where ϕ_λ is the polarization angle at the wavelength λ and ϕ_0 is the intrinsic polarization angle at $\lambda = 0$. The data are not sufficient to resolve the n–π ambiguity, so $n = 0$ is assumed.

The RM map is shown in Fig. 31, along with the error computed from the linear fit procedure. The area of Fermi bubbles looks to have low RMs, negative in the north lobe and positive in the south one. The bubbles are overlapped by higher RM regions generated by structures in the foreground. The high RMs generated by the H II region of the nearby ζ Oph are obvious, as are the local ring-like structure G353–34 and the arc of stronger RMs at the southern and western edge of the H I supershell GSH 006–15+7 analysed by Thomson et al. (2018). The latter protrudes from the Sagittarius arm some 1.5 kpc from the Sun. The Orion area and the Gum Nebula also stand out.

It is worth mentioning that in areas of strong depolarization the lambda-squared law fails, so these RMs are underestimated.

7 SCIENTIFIC RESULTS FROM S-PASS

A very diverse range of astrophysics research has been conducted with S-PASS data so far, from the study of the local ISM to CMB foregrounds and the Cosmic Web, via the structure of our Galaxy (to mention only a few highlights). In Table 3, we give a list of the articles published to date that employ S-PASS data. Further details can be found in each individual article. More work, not reported here, is in progress and to be published soon.

8 DATA RELEASE

With this article, we make the S-PASS maps publicly available. More specifically, we will release the following maps, in both HEALPIX format and Aitoff projection:

(i) Stokes Q,
(ii) Stokes U,
(iii) Stokes I,
(iv) Stokes Q, U pixel sensitivity,
(v) RM map,
(vi) RM error map.

Data will be made available on the website https://sites.google.com/inaf.it/spass and on the Legacy Archive for Microwave Background Data Analysis (LAMBDA)[3] website.

9 SUMMARY AND CONCLUSIONS

We have observed the entire southern sky at Dec. $< -1^\circ$ at 2.3 GHz with the Parkes Radio Telescope, realizing a detailed polarization map with a resolution of 8.9 arcmin that preserves information on all angular scales, including the overall mean emission of Stokes Q and U. Given the high resolution (for a single-dish telescope) of our measurements, our data encompass a spatial dynamic range of some 1200, one of the largest ever achieved in similar studies. The mean sensitivity of S-PASS on a beam-size scale is 0.81 mK. We account for systematic errors, including ground contamination (the largest source of uncertainty), to an accuracy of 0.35 mK.

One of the major goals of the survey was to preserve the global offset of Stokes Q and U. This has been achieved with a novel scanning strategy based on long azimuth scans at the EL of the South Celestial Pole at the telescope location taken at both east and west azimuths, combined with a map-making procedure that makes use of a basket-weaving technique as well as parallactic angle modulation. This procedure has been tested with realistic simulations and was shown to be able to recover the global mean emission with an accuracy better than 0.5 per cent.

Simulations demonstrate that the reconstruction error of our technique adds negligible error even in low-emission areas ($L <$ 20 mK) and achieves S/N $>$ 50 elsewhere. This ensures high-quality data, with the error budget led by instrumental noise and flux calibration accuracy with negligible additional errors.

The survey has been successful in unveiling the polarized emission from the Galactic disc and the disc–halo transition region, previously hidden by Faraday depolarization at lower frequencies. This allows improved studies of Galactic magnetism with diffuse emission, including large-scale Galactic structure, the Galactic

[3] https://lambda.gsfc.nasa.gov/

magnetic field and ISM turbulence. A number of scientific analyses have already been conducted and more are possible in a number of diverse science areas.

We find that the mean polarized emission at 2.3 GHz is 29 mK and the typical emission in low-emission areas is ∼13 mK. 50 per cent of the S-PASS area has polarized emission fainter than 23.6 mK and 98.6 per cent of the pixels have S/N > 3.

We also computed the RM map of the diffuse emission, combining S-PASS with archival higher frequency maps from *WMAP* and *Planck* at the locations where *WMAP* and *Planck* are consistent. The resolution of this map is 2°, with sensitivity limited by the poor S/N ratio of the high-frequency data. We expect to obtain a higher resolution and higher sensitivity RM map when S-PASS is combined with the upcoming GMIMS southern surveys.

Although not the primary goal of S-PASS, the data have also been used to generate Stokes *I* images with rms error set by the confusion limit (9 mK). The offset calibration, impossible to constrain in total intensity with our observing technique, has been obtained using archival data of absolutely calibrated observations of the south celestial pole.

ACKNOWLEDGEMENTS

This work has been carried out in the framework of the S-band Polarization All Sky Survey collaboration (S-PASS). We thank John Reynolds and Andrew Hunt for modifying the Parkes drive software and turning an idea in our mind into reality, Warwick Wilson for creating the backend configuration required by S-PASS, the whole Parkes Operations team, who made observing with such a complicated set-up smooth, and The Dish for having behaved seamlessly despite being nearly 50 years old. We thank team member Stefano Cortiglioni for his contribution. We thank Tom Landecker for fruitful discussions on brightness-temperature calibration and Nicoletta Krachmalnicoff for generating the PSM Stokes *I* map. We thank the referee for constructive comments. The Parkes radio telescope is part of the Australia Telescope National Facility, which is funded by the Commonwealth of Australia for operation as a National Facility managed by CSIRO. This work was partly funded by ASI under the project ASI I/016/07/0. The Dunlap Institute is funded through an endowment established by the David Dunlap family and the University of Toronto. RMC was the recipient of an Australian Research Council Future Fellowship (FT110100108). BMG acknowledges the support of the Natural Sciences and Engineering Research Council of Canada (NSERC) through grant RGPIN-2015-05948, and of the Canada Research Chairs program. XHS is supported by the National Natural Science Foundation of China under grant no. 11763008. MH acknowledges funding from the European Research Council (ERC) under the European Union Horizon 2020 research and innovation programme (grant agreement No 772663. We acknowledge the use of the MIRIAD package (Sault et al. 1995). We acknowledge the use of the PSM, developed by the Component Separation Working Group (WG2) of the Planck Collaboration. The Wisconsin H–Alpha Mapper and its sky survey have been funded primarily through awards from the US National Science Foundation. This research made use of Montage. It is funded by the National Science Foundation under Grant Number ACI-1440620, and was previously funded by the National Aeronautics and Space Administration's Earth Science Technology Office, Computation Technologies Project, under Cooperative Agreement Number NCC5-626 between NASA and the California Institute of Technology.

REFERENCES

Bennett C. L. et al., 2013, ApJS, 208, 20
Bernardi G., Carretti E., Cortiglioni S., Sault R. J., Kesteven M. J., Poppi S, 2003, ApJ, 594, L5
Bersanelli M., Bensadoun M., de Amici G., Levin S., Limon M., Smoot G. F., Vinje W., 1994, ApJ, 424, 517
Brentjens M. A., de Bruyn A. G., 2005, A&A, 441, 1217
Broten N. W., MacLeod J. M., Vallee J. P., 1988, ApSS, 141, 303
Brouw W. N., Spoelstra T. A. Th., 1976, A&AS, 26, 129
Brown S., Rudnick L., 2011, MNRAS, 412, 2
Brown S. et al., 2017, MNRAS, 468, 4246
Burn B. J., 1966, MNRAS, 133, 67
Carretti E., Cortiglioni S., Sbarra C., Tascone R., 2004, A&A, 420, 437
Carretti E., Haverkorn M., McConnell D., Bernardi G., McClure-Griffiths N. M., Cortiglioni S., Poppi S., 2010, MNRAS, 405, 1670
Carretti E., McConnell D., McClure-Griffiths N. M., Bernardi G., Cortiglioni S., Poppi S., 2005, MNRAS, 360, L10
Carretti E. et al., 2013a, Nature, 493, 66
Carretti E. et al., 2013b, MNRAS, 430, 1414
Delabrouille et al., 2013, A&A, 553, A96
Dickey J. M., 2013, in Oswalt T., Gilmore G., eds, Chapter 11: Planets, Stars, and Stellar Systems Volume 5, Galactic Structure and Stellar Populations. Springer, Dordrecht
Emerson D. T., Gräve R., 1988, A&A, 190, 353
Farnes J. S., Gaensler B. M., Carretti E., 2014, ApJS, 212, 15
Gaensler B. M. et al., 2011, Nature, 478, 214
Gardner F. F., Whiteoak J. B., Morris D., 1975, Australian Journal of Physics Astrophysical Supplement, 35, 1
Górski K. M., Hivon E., Banday A. J., Wandelt B. D., Hansen F. K., Reinecke M., Bartelmann M., 2005, ApJ, 622, 759
Haffner L. M. et al., 2010, in Kothes R., Landecker T. L., Willis A. G., eds, ASP Conf. Ser. Vol. 438, The Dynamic Interstellar Medium: A Celebration of the Canadian Galactic Plane Survey. Astron. Soc. Pac., San Francisco, p. 388
Haverkorn M., 2015, in Lazarian A., e Gouveia Dal Pino E. M., Melioli C., eds, Magnetic Fields in Diffuse Media, ApSS Library, Vol. 407, Springer-Verlag, Berlin, Heidelberg, p. 483
Herron C. A., Geisbuesch J., Landecker T. L., Kothes R., Gaensler B. M., Lewis G. F., McClure-Griffiths N. M., Petroff E., 2017, ApJ, 835, 210
Herron C. A. et al., 2018, ApJ, 855, 29
Iacobelli M. et al., 2014, A&A, 566, A5
Jansson R., Farrar G. R., 2012, ApJ, 757, 14
Jones M. E., et al., 2018, MNRAS, 480, 3224
Krachmalnicoff N., Baccigalupi C., Aumont J., Bersanelli M., Mennella A., 2016, A&A, 588, A65
Krachmalnicoff N. et al., 2018, A&A, 618, A166
Lamee M., Rudnick L., Farnes J. S., Carretti E., Gaensler B. M., Haverkorn M., Poppi S., 2016, ApJ, 829, 5
Loi F. et al., 2017, MNRAS, 472, 3605
Mao S. A., Gaensler B. M., Haverkorn M., Zweibel E. G., Madsen G. J., McClure-Griffiths N. M., Shukurov A., Kronberg P. P., 2010, ApJ, 714, 1170
McKinley B. et al., 2018, MNRAS, 474, 4056
Meyers B. W. et al., 2017, PASA, 34, e013
Murgia M. et al., 2016, MNRAS, 461, 3516
Nicastro F. et al., 2018, Nature, 558, 406
Oppermann N. et al., 2015, A&A, 575, 118
Page L. et al., 2007, ApJS, 170, 335
Perley R. A., Butler B. J., 2013, ApJS, 206, 16
Planck Collaboration, 2018, A&A, preprint (arXiv:1807.06207)
Poidevin F. et al., 2018, in 13th Rencontres du Vietnam. preprint (arXiv: 1802.04594)
Purcell C. R. et al., 2015, ApJ, 804, 22
Reynolds J. E., 1994, ATNF Tech. Doc. Ser. 39.3040
Robitaille J.-F., , Scaife A. M. M., Carretti E., Haverkorn M., Crocker R. M., Kesteven M. J., Poppi S., Staveley-Smith L., 2018, A&A, 617, A101
Robitaille J.-F. et al., 2017, MNRAS, 468, 2957

Sault R. J., Teuben P. J., Wright M. C. H., 1995, in Shaw R., Payne H. E., Hayes J. J. E., eds, ASP Conf. Ser. Vol. 77, Astronomical Data Analysis Software and Systems IV. Astron. Soc. Pac., San Francisco, p. 433
Schnitzeler D. H. F. M., Carretti E., Wieringa M. H., Gaensler B. M., Haverkorn M., Poppi S., 2019, MNRAS, 485, 1293
Su M., Slatyer T. R., Finkbeiner D. P., 2010, ApJ, 724, 1044
Sun X. H., Gaensler B. M., Carretti E., Purcell C. R., Staveley-Smith L., Bernardi G., Haverkorn M., 2014, MNRAS, 437, 2936
Sun X. H., Reich W., Waelkens A., Enßlin T. A., 2008, A&A, 477, 573
Testori J. C., Reich P., Reich W., 2008, A&A, 484, 733
Thomson A. et al., 2018, MNRAS, 479, 5620
Vacca V. et al., 2018, MNRAS, 479, 776
Vernstrom T., Gaensler B. M., Brown S., Lenc E., Norris R. P., 2017, MNRAS, 467, 4914
Vidal M., Dickinson C., Davies R. D., Leahy J. P., 2015, MNRAS, 452, 656
Wardle J. F. C., Kronberg P. P., 1974, ApJ, 194, 249
Wolleben M., Landecker T. L., Hovey G. J., Messing R., Davison O. S., House N. L., Somaratne K. H. M. S., Tashev I., 2010, AJ, 139, 1681
Wolleben M., Landecker T. L., Reich W., Wielebinski R., 2006, A&A, 448, 411
Wolleben M. et al., 2009, in Strassmeier K.G., Kosovichev A.G., Beckman J.E., eds, IAU Symp. 259, Cosmic Magnetic Fields: From Planets, to Stars and Galaxies, Cambridge University Press, Cambridge. p. 89.
Wolleben M. et al., 2019, AJ, in press

APPENDIX A: STOKES *Q* AND *U* SCANS OFFSET CALIBRATION

This section presents the equations to find the best offset set for Stokes Q and U scans.

Let $\boldsymbol{Y}_i$ be the polarization vector (Q, U) of the ith piece of data measured in the instrument reference frame:

$$\boldsymbol{Y}_i = \begin{bmatrix} Q_{m,i} \\ U_{m,i} \end{bmatrix}, \tag{A1}$$

$\boldsymbol{X}_i$ the polarization vector of sky emission in the sky reference frame:

$$\boldsymbol{X}_i = \begin{bmatrix} Q_i \\ U_i \end{bmatrix}, \tag{A2}$$

$\boldsymbol{A}_{is}$ the offsets of Q and U of the scan is:

$$\boldsymbol{A}_{is} = \begin{bmatrix} A_{is}^{Q} \\ A_{is}^{U} \end{bmatrix} \tag{A3}$$

and $\boldsymbol{R}(\theta)$ the 2D rotation matrix between two local 2D reference frames centred on the pointing direction rotated by the angle θ, so that $\boldsymbol{R}(-2\phi)$ is the rotation matrix to convert Q and U from the instrument to the sky reference frame (ϕ is the parallactic angle).

For the sample i taken in the scan is,

$$\boldsymbol{X}_i = \boldsymbol{R}(-2\phi_i)(\boldsymbol{Y}_i + \boldsymbol{A}_{is}). \tag{A4}$$

The best offset set is obtained by minimizing the square differences between the sky emission observed in the same pixel with different scans:

$$\begin{aligned} S^2 &= \sum_{is=2}^{n_s} \sum_{ik=1}^{is-1} \sum_{p=1}^{n_p^{is,ik}} w_p \left| \boldsymbol{X}_{p,is} - \boldsymbol{X}_{p,ik} \right|^2 \\ &= \sum_{is=2}^{n_s} \sum_{ik=1}^{is-1} \sum_{p=1}^{n_p^{is,ik}} w_p \left| \left(\boldsymbol{R}_{p,is} \boldsymbol{Y}_{p,is} - \boldsymbol{R}_{p,ik} \boldsymbol{Y}_{p,ik} \right) + \left(\boldsymbol{R}_{p,is} \boldsymbol{A}_{is} - \boldsymbol{R}_{p,ik} \boldsymbol{A}_{ik} \right) \right|^2, \end{aligned} \tag{A5}$$

where n_s is the number of scans, $n_p^{is,ik}$ the number of pixels where the two scans is and ik cross, $\boldsymbol{Y}_{p,ix}$ the polarized emission vector at the pixel p observed with the scan ix, $\boldsymbol{R}_{p,ix} = \boldsymbol{R}(-2\phi_{p,ix})$, $\boldsymbol{A}_{ix}$ the offset of the scan ix and w_p a weight for pixel p. In this work we have used $w_p = 1$, but it is included here to give the most general formulation.

The minimization is performed compared with all the $2n_s$ free parameters $\boldsymbol{A}_i$,

$$\frac{\partial S^2}{\partial A_i^Q} = 0, \quad \text{for } i = 1, n_s, \tag{A6}$$

$$\frac{\partial S^2}{\partial A_i^U} = 0, \tag{A7}$$

or, in a more compact format,

$$\frac{\partial S^2}{\partial \boldsymbol{A}_i} = \begin{bmatrix} 0 \\ 0 \end{bmatrix} \qquad \text{for } i = 1, n_s, \tag{A8}$$

where we define

$$\frac{\partial}{\partial \boldsymbol{A}_i} = \begin{bmatrix} \frac{\partial}{\partial A_i^Q} \\ \frac{\partial}{\partial A_i^U} \end{bmatrix}. \tag{A9}$$

Let us define

$$\boldsymbol{D}_{p,is,ik} = \left(\boldsymbol{R}_{p,is}\boldsymbol{Y}_{p,is} - \boldsymbol{R}_{p,ik}\boldsymbol{Y}_{p,ik}\right) + \left(\boldsymbol{R}_{p,is}\boldsymbol{A}_{is} - \boldsymbol{R}_{p,ik}\boldsymbol{A}_{ik}\right) \tag{A10}$$

and D_Q, D_U its two components.

Considering that

$$\frac{\partial}{\partial A_i^Q}\left(\boldsymbol{R}_{p,j}\boldsymbol{A}_j\right) = \begin{bmatrix} R^{11}_{p,j}\delta_{i,j} \\ R^{21}_{p,j}\delta_{i,j} \end{bmatrix} = \begin{bmatrix} \cos(-2\phi_{p,j})\,\delta_{i,j} \\ -\sin(-2\phi_{p,j})\,\delta_{i,j} \end{bmatrix}, \tag{A11}$$

$$\frac{\partial}{\partial A_i^U}\left(\boldsymbol{R}_{p,j}\boldsymbol{A}_j\right) = \begin{bmatrix} R^{12}_{p,j}\delta_{i,j} \\ R^{22}_{p,j}\delta_{i,j} \end{bmatrix} = \begin{bmatrix} \sin(-2\phi_{p,j})\,\delta_{i,j} \\ \cos(-2\phi_{p,j})\,\delta_{i,j} \end{bmatrix}, \tag{A12}$$

the partial derivates of each term of equation (A5) are

$$\frac{\partial}{\partial A_i^Q}\left|\boldsymbol{D}_{p,is,ik}\right|^2 = 2\left[\left(\boldsymbol{R}^{\mathrm{T}}_{p,is}\boldsymbol{D}_{p,is,ik}\right)_Q\delta_{i,is} - \left(\boldsymbol{R}^{\mathrm{T}}_{p,ik}\boldsymbol{D}_{p,is,ik}\right)_Q\delta_{i,ik}\right], \tag{A13}$$

$$\frac{\partial}{\partial A_i^U}\left|\boldsymbol{D}_{p,is,ik}\right|^2 = 2\left[\left(\boldsymbol{R}^{T}_{p,is}\boldsymbol{D}_{p,is,ik}\right)_U\delta_{i,is} - \left(\boldsymbol{R}^{T}_{p,ik}\boldsymbol{D}_{p,is,ik}\right)_U\delta_{i,ik}\right], \tag{A14}$$

where the subscripts $_Q$ and $_U$ denote the Q and U components and T the transpose matrix, or, using the compact format of equations (A9),

$$\frac{\partial}{\partial \boldsymbol{A}_i}\left|\boldsymbol{D}_{p,is,ik}\right|^2 = 2\left[\left(\boldsymbol{R}^{\mathrm{T}}_{p,is}\boldsymbol{D}_{p,is,ik}\right)\delta_{i,is} - \left(\boldsymbol{R}^{\mathrm{T}}_{p,ik}\boldsymbol{D}_{p,is,ik}\right)\delta_{i,ik}\right]. \tag{A15}$$

From equations (A5) and (A15), the solving equation (A9) can be written as

$$\sum_{is\neq i}\sum_{p=1}^{n_p^{is,i}} w_p\left(\boldsymbol{A}_i - \boldsymbol{R}^{\mathrm{T}}_{p,i}\boldsymbol{R}_{p,is}\boldsymbol{A}_{is} + \boldsymbol{Y}_{p,i} - \boldsymbol{R}^{\mathrm{T}}_{p,i}\boldsymbol{R}_{p,is}\boldsymbol{Y}_{p,is}\right) = \begin{bmatrix} 0 \\ 0 \end{bmatrix} \qquad \text{for } i = 1, n_s. \tag{A16}$$

Rearranged to focus on the variables $\boldsymbol{A}_i$ to solve for, it turns into n_s pairs of equations:

$$\left(\sum_{is\neq i}\sum_{p=1}^{n_p^{is,i}} w_p\right)\boldsymbol{A}_i + \sum_{is\neq i}\left(-\sum_{p=1}^{n_p^{i,is}} w_p\boldsymbol{R}^{\mathrm{T}}_{p,i}\boldsymbol{R}_{p,is}\right)\boldsymbol{A}_{is} = \sum_{is\neq i}\sum_{p=1}^{n_p^{is,i}} w_p\left(\boldsymbol{R}^{\mathrm{T}}_{p,i}\boldsymbol{R}_{p,is}\boldsymbol{Y}_{p,is} - \boldsymbol{Y}_{p,i}\right) \qquad \text{for } i = 1, n_s, \tag{A17}$$

which is the system of $2n_s$ linear equations to solve to find the best set of offset values $\boldsymbol{A}_i$.

It can also be written in matrix form as

$$\mathbf{M}\cdot\mathbf{A} = \mathbf{B}, \tag{A18}$$

where $\mathbf{M}$ is the $n_s \times n_s$ matrix with elements that are the 2×2 matrixes

$$\boldsymbol{M}_{i,i} = \sum_{is\neq i}\sum_{p=1}^{n_p^{is,i}} w_p\boldsymbol{I}, \tag{A19}$$

$$\boldsymbol{M}_{i,is} = -\sum_{p=1}^{n_p^{i,is}} w_p\boldsymbol{R}^{\mathrm{T}}_{p,i}\boldsymbol{R}_{p,is}, \qquad \text{for } i \neq is, \tag{A20}$$

$\boldsymbol{A}_i$ is defined in equation (A3), and

$$\boldsymbol{B}_i = \sum_{is\neq i}\sum_{p=1}^{n_p^{is,i}} w_p\left(\boldsymbol{R}^{\mathrm{T}}_{p,i}\boldsymbol{R}_{p,is}\boldsymbol{Y}_{p,is} - \boldsymbol{Y}_{p,i}\right). \tag{A21}$$

APPENDIX B: STOKES *I* SCAN OFFSET CALIBRATION

The equations to estimate the best set of offsets for Stokes I scans are obtained as for Stokes Q and U, except that the two-component vectors $\boldsymbol{Y}_i$, $\boldsymbol{X}_i$ and $\boldsymbol{A}_{is}$ are replaced by the scalars y_i, x_i and A_{is}, and the rotation matrix $\boldsymbol{R}$ with the scalar unity 1.

Following the same steps, one obtains a system of n_s equations to solve:

$$\left(\sum_{is\neq i}\sum_{p=1}^{n_p^{is,i}} w_p\right) A_i + \sum_{is\neq i}\left(-\sum_{p=1}^{n_p^{i,is}} w_p\right) A_{is} = \sum_{is\neq i}\sum_{p=1}^{n_p^{is,i}} w_p \left(y_{p,is} - y_{p,i}\right) \qquad \text{for } i = 1, n_s. \tag{B1}$$

In matrix form:

$$\mathbf{M}\cdot\mathbf{A} = \mathbf{B}, \tag{B2}$$

where $\mathbf{M}$ is the $n_s \times n_s$ matrix of elements

$$\boldsymbol{M}_{i,i} = \sum_{is\neq i}\sum_{p=1}^{n_p^{is,i}} w_p, \tag{B3}$$

$$\boldsymbol{M}_{i,is} = -\sum_{p=1}^{n_p^{i,is}} w_p \qquad \text{for } i \neq is \tag{B4}$$

and the n_s-element vector

$$\boldsymbol{B}_i = \sum_{is\neq i}\sum_{p=1}^{n_p^{is,i}} w_p \left(y_{p,is} - y_{p,i}\right). \tag{B5}$$

It is worth noting that this system is degenerate because of the lack of parallactic angle modulation that Q and U benefit from (see main text). It is solved through the singular-value decomposition (SVD) method, a powerful tool to solve ill-conditioned systems.

This paper has been typeset from a TEX/LATEX file prepared by the author.